1 **Title: Multi-modal mass spectrometry imaging reveals single-cell metabolic states in mammalian**

2 **liver**

3

4

5 Authors:

6 Hua Tian[1,*,#], Presha Rajbhandari[2, #], Jay Tarolli[3], Aubrianna M. Decker[2], Taruna V. Neelakantan[4], Tina

7 Angerer[5,6], Fereshteh Zandkarimi[4], Jacob Daniels[2], Helen Remotti[7], Gilles Frache[5], Nicholas Winograd[1],

8 Brent R. Stockwell[2,4, *]

9

10 1. Department of Chemistry, Pennsylvania State University, University Park, PA 16802, US

11 2. Department of Biological Sciences, Columbia University, New York, NY 10023, US

12 3. Ionpath Inc., Menlo Park, CA 94025, US

13 4. Department of Chemistry, Columbia University, New York, NY 10027, US

14 5. The Luxembourg Institute of Science and Technology, L-4362 Esch-sur-Alzette, Luxembourg

15 6. Department of Pharmaceutical Biosciences, Uppsala University, SE-751 05 Uppsala, Sweden

16 7. Department of Pathology, Columbia University, New York, NY 10032, US

17

18

19

20

21

22

23

24

25

26

27

28

29

30

31

* Corresponding authors: Hua Tian: hut3@psu.edu; Brent R. Stockwell: bstockwell@columbia.edu
# These authors contributed equally to this work
Lead contact for resource requirement: hut3@psu.edu

Summary

We have developed a powerful workflow to imaging endogenous metabolism in single cells on frozen tissue, allowing us to discover new cell subtypes in human liver. Performing spatially integrated multi-omics in single cells within tissues is at the leading frontier in biology but has been prevented by technological challenges. We developed a critical new technology, cryogenic water cluster ion beam secondary ion mass spectrometry imaging $((H_2O)_{n>28K}$-GCIB-SIMS)) at 1 µm single-cell resolution. This allowed us to perform multi-modal mass spectrometry imaging (MSI) to detect metabolites, lipids, and proteins in single cells within functional liver zones and diverse cell types in the native tissue state. Our workflow utilizes the desorption electrospray ionization (DESI) mass spectrometry imaging (MSI) to build a reference map of metabolic heterogeneity and zonation across liver functional units. Then cryogenic $(H_2O)_{n>28K}$-GCIB-SIMS and C_{60}-SIMS integrated metabolomics, lipidomic and proteomics, - characterizing the metabolic state in single cells on the same tissue section. We found for the first time that lipids and metabolites can classify liver metabolic zones and liver cell types beyond histological and protein-marker annotation. This provides a multi-modal workflow to define single-cell states in normal physiology and disease in mammalian tissue.

Key words: Single-cell spatial omics; Mass spectrometry imaging (MSI); Water cluster ion beam secondary ion mass spectrometry imaging $((H_2O)_{n>28K}$-GCIB-SIMS)); Desorption electrospray ionization (DESI); Metabolic states; Liver tissue; Molecular and cellular heterogeneity

Introduction

Recent developments in spatial omics technologies have improved how cellular heterogeneity and tissue organization can be assessed. Efforts such as Human Biomolecular Atlas Program (HuBMAP) (Hu, 2019), Human Tumor Atlas Network (HTAN) (Rozenblatt-Rosen et al., 2020) and Kidney Precision Medicine Project (KPMP(El-Achkar et al., 2021)) aim to map the diversity of cell types and subtypes and their biomarkers to characterize cell types within anatomical structures in healthy and disease tissues at single cell resolution (Borner et al., 2021). While spatial transcriptomics and proteomics have been the most common technologies implemented for such efforts, spatial metabolomics could illuminate the crucial role of effector metabolites that reflect the network of upstream molecules at genomic, transcriptomic and proteomic levels, but have been difficult to detect (Eberlin, 2014; Hickey et al., 2022; Radtke et al., 2020). Mass spectrometry imaging (MSI) is the primary method for spatial metabolomics, enabling multiplexed mapping of untargeted and targeted molecular networks within cells and tissue. Widely used MSI technologies include desorption electrospray ionization (DESI) (Takats et al., 2005) and matrix-assisted laser desorption ionization (MALDI) (Caprioli et al., 1997; Winograd, 2018). DESI is an ambient ionization technique with preferential ionization and characterization of metabolites and lipids at spatial resolution as high as 30 µm (Eberlin, 2014). MALDI is utilized for lipids, abundant proteins, and metabolites with a suitable matrix at an achievable spatial resolution of 5-10 µm (Djambazova et al., 2020).

However, the practical application of MSI at a single-cell resolution has not been possible. First, detection limits hinder imaging of low concentration biomolecules as the amount of material sampled is decreased exponentially within smaller pixels. Second and critically, cryogenic analysis of native cell states is not widely applicable to different MSI tools, which is essential to preserve the pristine chemical gradients in tissue, especially for dynamic and transient metabolites. Finally, due to the incompatibility of sample preparation and difficulty in preserving dynamic metabolic gradients (Tian et al., 2021), it is challenging to acquire multi-omic data within the same tissue section, or to spatially co-localize molecules at single cell level.

We have solved these long-standing problems by developing a buncher-time-of-flight (ToF) SIMS coupled with high voltage water cluster ion beam, $(H_2O)_{n(n>28K)}$-GCIB and establishing a dual-SIMS workflow. The first step takes advantage of intact biomolecular imaging (up to m/z 5000) at an achievable

94   spatial resolution of ~1 µm, using a newly designed GCIB operating at ~70 kV (Sheraz et al., 2019; Tian
95   et al., 2021; Tian et al., 2019). Along with cryogenic sample handling, frozen-hydrated biosamples are
96   transferred in a contamination-free nitrogen atmosphere and images at near-nature status (at 100 K). Cell-
97   type-specific and tissue structure proteins are mapped in the same sample stained with a panel of
98   lanthanides-conjugated antibodies using C_{60}-SIMS at the spatial resolution of 1 µm. This development
99   allowed us for the first time to simultaneously map multiple metabolites, lipids, and peptides in the same
100 tissue section at single-cell resolution, with high sensitivity (Taylor et al., 2021).

101

102 We applied our pipeline to liver tissue, which is a metabolic hub performing diverse and critical functions,
103 including uptake and storage of nutrients, metabolism, bile secretion, detoxification, protein synthesis,
104 and immune functions (Trefts et al., 2017). To perform these functions, the hepatic parenchyma exhibits
105 metabolic zonation based on the gradient of oxygen-and-nutrient-rich blood along the portal triad (PT) to
106 central vein (CV) axis. The periportal (PP) region surrounding the PT receives a maximum amount of
107 nutrients and oxygen, and is a key site for oxidative metabolism, including β-oxidation, gluconeogenesis,
108 bile formation, and cholesterol synthesis. The pericentral (PC) region surrounding the CV receives less
109 oxygen and nutrients, and is a key site for detoxification, ketogenesis, lipogenesis, glycolysis, glycogen
110 synthesis and glutamine synthesis(Gebhardt and Matz-Soja, 2014; Kietzmann, 2017).

111

112 Although histologically hepatocytes in different zones appear homogeneous using conventional imaging
113 methods, these regions are metabolically distinct, shown by the zonal preferences of metabolic enzymes
114 involved in oxidative energy, carbohydrate, lipid, and nitrogen metabolism, including
115 carbamoylphosphate synthetase (CPS1), glutamine synthetase (GS) and cytochrome P450, family 2,
116 subfamily AE, polypeptide1 (Cyp2ae1) (Lamers et al., 1989). The heterogeneity of the liver extends to
117 the cellular level, where multiple cell types are organized in a structured manner to carry out essential
118 liver functions. Within the liver parenchyma, hepatocytes make up 70% of the cell population and are
119 metabolically heterogeneous along the porto-central axis. Non-parenchymal cells, including macrophages
120 (Kupffer cells), liver sinusoidal endothelial cells, and hepatic stellate cells, are located within the hepatic
121 sinusoids and play a critical role in interacting with and regulating parenchymal cells(Aizarani et al.,
122 2019). While liver zonation and function has mainly been explored with immunohistochemistry and single
123 cell spatial transcriptomics(Gebhardt and Matz-Soja, 2014; Halpern et al., 2017), measurement of lipids
124 and metabolites, the effector molecules of metabolic pathways, is lacking.

125

126   Here, we present a multimodal MSI approach centered on DESI, $(H_2O)_n$-GCIB-SIMS and C_{60}-SIMS for

127   mapping of untargeted, endogenous, unlabeled metabolites and lipids, and targeted protein markers within

128   anatomical structure and cell types, providing a powerful new understanding of metabolic zonation and

129   cell type identity in mouse and human liver. This workflow is complemented and validated by histologic

130   (hematoxylin and eosin (H&E)) staining for anatomical structure annotation within liver and multimodal

131   image alignment, RNAScope for mRNA transcript profiling of landmark genes (Wang et al., 2012) for

132   zonation marking and antibody validation, and MALDI Orbitrap MSI. Moreover, ultra-high performance

133   liquid chromatography (UPLC) coupled with electrospray ionization (ESI) tandem mass spectrometry

134   (MS/MS) is adapted for lipid confirmation in DESI and SIMS experiments. Heterogeneities in liver tissue

135   were detected by the combination of metabolites, lipids, and proteins in human and mouse liver, including

136   sex-specific zonation patterns, functional-specific zonation, and metabolic states of different cell types.

137   We found for the first time that lipid and metabolite composition classify liver zonation and cell types, as

138   well as novel cell subtypes that have not previously been detected by protein or RNA markers. Thus, this

139   new technology for single-cell multi-omic imaging allows for unprecedented understanding metabolic cell

140   states and cell identity.

141

142   **Results and discussion**

143   *Multimodal imaging centered on novel mass spectrometry imaging technologies reveals a spatial multi-*

144   *omic (metabolite, lipid and protein) atlas of liver tissue*

145   To comprehensively assess the spatial organization of liver tissue with regard to its cellular and metabolic

146   and lipidomic heterogeneity, we performed multi-modal imaging on consecutive tissue sections of mouse

147   and human liver using DESI, H&E staining, SIMS, and RNAscope, followed by computational data

148   processing for cellular and structure segmentation, omics integration and discriminant analysis.

149   Histological features of the H&E tissue sections were analyzed to guide MSI, with a focus on the PT and

150   CV regions.

151

152   DESI was employed to image an entire tissue section at a spatial resolution of 40 µm in both positive and

153   negative ion modes. More than 100 lipid and metabolite features were extracted, and ion species localized

154   to the PP and PC regions (Figure 1a) were identified. A region containing both PT and CV was selected

155   on consecutive tissue sections for single-cell resolution SIMS imaging in a frozen-hydrated state (Figure

156 1B). We implemented a novel technological development using a three-step process: first, cryogenic

157 $(H_2O)_n$-GCIB-SIMS was performed to localize >100 lipid and metabolites in a pristine native environment

158 at 3 µm per pixel, followed by staining with a panel of lanthanide-labeled antibodies specific to liver

159 biology (Table S1 and S2) on the same tissue section. C_{60}-SIMS was then utilized to image metal-labeled

160 antibodies to map cell-types, cell states, and structure-specific protein markers at 1 µm per pixel. As

161 $(H_2O)_n$-GCIB-SIMS removes about 100 nm material from the tissue surface, the antibody markers stain

162 the same cells as those from which lipids and metabolites are detected. This unique approach facilitated

163 image alignment and cell segmentation to register untargeted metabolites and lipids and targeted proteins

164 to single cells on the same tissue section, elucidating biomolecular complexity within different cell types

165 directly in their tissue content without dissociation, which is otherwise not possible in single-cell

166 multimodal image integration.

167

168 To validate DESI and SIMS imaging in terms of assignment of zones and cell types, RNAScope was

169 performed on a consecutive tissue section for transcriptomic analysis of several zonation and cell-type-

170 specific markers. To validate ion species assignment by accurate mass and fragmentation pattern, we

171 performed (a) MALDI on an Orbitrap, performed on the serial sections for in situ MS/MS analysis, and

172 (b) lipidomics analysis using UPLC with ion mobility time-of-flight MS^E ($HDMS^E$) data-independent

173 acquisition and analysis (Figure 1C).

174

175 With 2D/3D image reconstruction, molecular and cellular heterogeneity was visualized (Figure 1E),

176 showing distinct molecular clusters in different areas and Correlation of proteins and metabolites and

177 lipids in the PT region in human liver.

178

179 *DESI MSI reveals metabolic zonation-specific metabolites and lipids in mouse liver*

180 To evaluate metabolite and lipid distribution with metabolic zones, we first examined histology of mouse

181 liver tissue sections obtained from six different mice (3 male and 3 female). H&E-stained images were

182 annotated to identify the PT and CV regions, showing uniform distribution patterns within the tissue

183 (Figure 2 Ai, S1a). The annotation was then validated by transcript and protein markers targeting

184 metabolic enzymes that are specific to PP and PC regions(Lamers et al., 1989). For example, Albumin

185 (*Alb*) was concentrated in the PP region, and Glutamine Synthetase (*Glul*) was localized in the PC region

186 using RNAScope, respectively (Figure 2 Aii, S1b). The distributions were consistent with the previous

187 work(Halpern et al., 2017), however, we noted sex-linked differences. *Alb* was concentrated more around

188 the PP zone in male mice, whereas it expanded towards the central vein in female mice. *Glul* expression

189 has been previously shown to exhibit sex-specific variation in different mouse and rat strain(Sirma et al.,

190 1996); we observed a similar distribution pattern between male and female mice in the C57BL6 mouse

191 strain used in this study.

192

193 DESI imaging of mouse liver showed distinct mass spectra representing metabolites and lipids in both

194 positive and negative ion mode. In positive mode, ions corresponding to lipids from different classes,

195 including glycerophospholipids and glycerolipids were observed (Figure S2a, Table S3). In negative ion

196 mode, free fatty acids and small metabolites in a low m/z range (m/z 100-400), glycerophospholipids in

197 high m/z range (m/z 700-800) and conjugated bile acids were observed (Figure S2b, Table S3). In order

198 to extract PP and PC specific lipids and metabolites, we first sought to create a segmentation mask for

199 these regions within tissue sections. A few ion species (*m/z* 124.01, 280.23, 282.25, 306.07 and 309.28)

200 in negative ionization mode and *m/z* 534.29, 631.47, 734.57, 794.51, 802.5 and 852.55 in positive

201 ionization mode) exhibiting unique distribution patterns were used to perform bisecting k-means

202 clustering with Euclidean distance, within the SCiLS software platform. Spatial segmentation was

203 performed with edge-preserving denoising to remove pixel-to-pixel variability observed in MSI

204 datasets(Alexandrov et al., 2010). This resulted in PP and PC clusters in individual mouse liver tissue

205 sections in both positive and negative ion mode, shown as a segmentation map (Figure 2 Aiii and Av, S1c

206 and S1d).

207

208 We confirmed cluster specificity by comparing *Alb* and *Glul* transcript distribution with DESI

209 segmentation (Figure S1b, S1c and S1d). To identify lipids and metabolites that discriminate PC versus

210 PP clusters, we implemented a binary classifier—receiver operating characteristic (ROC)-area under the

211 curve (AUC) curve analysis(Bradley, 1997; Mandrekar, 2010). Each tissue-specific ion was evaluated for

212 its discriminating power, using a threshold of the area under the curve (AUC) >0.70 to be considered a

213 classifier. We observed that metabolites such as glutathione (GSH), taurine, and conjugated bile acids

214 were zonated in PP region (Figure 2B, S3c, S3d). Our results were complementary to previous results on

215 the metabolic gradients from PC to PP. Liver bile acids are primarily synthesized in PC hepatocytes, they

216 flow towards the bile duct and the enzymes cascade involved in bile acid biosynthesis is organized

217   spatially. In particular, the enzyme conjugating bile acids is abundant in PP region, where taurine also

218   comes in from blood supply(Halpern et al., 2017; Ikeda et al., 2012).

219

220   As noted, we observed sexual dimorphism in the distribution of several lipid species. While previous

221   studies have shown sex-specific differences in lipid metabolism, it has not been shown in the spatial

222   context within liver (Mittendorfer, 2005; Soares et al., 2017). Diacylglycerols (DGs) and free fatty acids

223   (FAs) are zonated in the PC region (Figure 2B, S3a, S3b), with the average ROC-AUC for individual DG

224   ions for males of >0.89 and females >0.7 (Figure 2B). Compared to females, male mice showed higher

225   amounts of DGs in PC versus PP zones (log$_2$ fold change of ~1.5 for males and 0.4 for females) (Figure

226   2C). Similar observations were made for FAs (Figure 2B, 2C, S3b). While some FAs such as FA(18:1),

227   FA(20:1), FA(18:3;O), FA(18:2) and FA(20:0) show high specificity for PC versus PP zone, with the

228   average ROC-AUC for individual ions for males of >0.88 and females >0.7 (Fig 2B), others such as

229   FA(18:2;O), FA(16:0), FA(22:5) and FA(20:2) exhibited higher specificity for PC zones in males versus

230   females, with the average ROC-AUC for individual ions for males of >0.73 and females <0.57. FA (20:0)

231   and FA(18:3;O) showed relatively higher abundance in PC versus PP in both male and female mice, and

232   FA(20:1) and FA(22:5) showed minimal differences between the regions in female mice (Figure 2C, S3b).

233

234   The PC region has previously been reported to exhibit a higher degree of lipogenesis, fatty acid synthesis

235   and acetyl CoA carboxylase expression than the PP zone(Guzman and Castro, 1989; Quistorff et al.,

236   1992). On the other hand, phospholipids, including phosphatidylcholine (PCs) and

237   lysophosphatidylcholine (LPCs), did not exhibit a specific pattern. Some lipids (e.g., PC(40:6)) showed

238   similar distribution between the PP and PC zones, while others (e.g., PC (36:5), PC (32:0), PC(34:1))

239   exhibited differential distributions between regions, or between regions and sexes (e.g., LPC(18:2),

240   LPC(18:0), LPC(16:0), PC(38:4) and PC(39:7)) (Figure 2B, 2C, S3e). Thus, while male and female mice

241   have histologically and morphologically similar livers, they are metabolically quite distinct.

242

243   *DESI MSI reveals zonation-specific metabolites and lipids in human liver*

244   The established DESI workflow was then performed on consecutive tissue sections from human liver

245   tissue. H&E staining was performed to assess tissue morphology and annotate PP and PC regions (Figure

246   2D). RNAScope was used to validate *Glul* staining, which unlike in mouse liver, appeared as dispersed

247   puncta around the CV region (Figure S4). This is likely due to lower expression of the gene in human

248   liver. Hence, PP and PC regions were annotated manually based on H&E staining (Figure 2D).

249

250   DESI imaging at 40 µm spatial resolution showed similar average mass spectra profiles in both positive

251   and negative ion modes compared to mouse liver (Figure S2c, S2d). Taurine-and-glycine-conjugated bile

252   acids were abundant in the PT and PP region, as well as in the septa connecting the neighboring PTs,

253   showing similar functional zonation between human and mouse liver (Figure 2D, S5b). The vasculature

254   were identified by the abundance of the marker, Heme B. Cholesterol, a precursor to bile acids, was

255   concentrated within PV and CV (Figure S5e). Sphingomyelins (SMs) including SM 34:1 were colocalized

256   with cholesterol (Figure 2D, S5e), where SMs are postulated to form hydrophobic lipid raft domains with

257   cholesterol, preventing hepatic damage from bile salts, and also playing a role in pathophysiology(Amigo

258   et al., 1999; Simons and Ehehalt, 2002). Similarly, stearoylcarnitine was localized in the PP region (Figure

259   2D), where acylcarnitines play an important role in transferring long-chain fatty acids to mitochondria for

260   β-oxidation(Longo et al., 2016). Several small metabolites and different lipid species exhibited differential

261   distributions in human tissue (Figure 2D, S5). FAs, DAGs and triglycerides (TAGs) exhibited distinct

262   distribution patterns, which unlike in mouse tissue, did not overlay well with the PC region (Figure 2D,

263   S5a, S5c, S5d). This could stem from the complexity of human liver, where metabolic gradients are more

264   dynamic and heterogeneous, based on a person's genetic profile and changes in gene expression and

265   metabolic-enzymes-based factors such as diet, hormones, gender and underlying pathology (Geisler and

266   Renquist, 2017; Kietzmann, 2017). Similarly, varied patterns of phospholipid species were observed

267   within the liver (Figure S5f).

268

269   In addition to 2D imaging of tissue sections, 3D DESI aids the visualization of the distribution of lipids

270   and metabolites within three-dimensional tissue structures and gradients with respect to tissue depth,

271   capturing branching of blood flow and anatomic structure. The resulting 3D model visualizing

272   differentially distributed lipids is shown in Supplementary Video 1.

273

274   *SIMS imaging delineates heterogeneities of multiple biomolecules and cell types at single-cell level in*

275   *mouse liver*

276   To associate lipids and metabolites with different types of cells in the liver, dual SIMS imaging at the

277   resolution of 1-3 µm was performed on a consecutive mouse liver sections. Guided by H&E stained

278   images, a region of interest (ROI) containing both CV and PV was selected (Figure 3 Ai) for $(H_2O)_{n(n=30k)}$-

279   GCIB-SIMS imaging in negative ion mode, mapping more than 100 lipids and metabolites in both mouse

280   and human liver. The highly heterogenous metabolites and lipids were observed around CV and PV,

281   including   nucleotides,   bile   acids,   glucose,   fatty   acids   (FA),   phosphatidylinositols   (PIs),

282   phosphatidylserines (PSs), lysophosphatidylserines (LPSs), phosphatidic acids (PAs), lysophosphatidic

283   acids (LPAs). PI(38:4) was highly concentrated in the PC region, and PS(40:6) distributed in

284   complimentary locations with an elevated concentration around the PP region. Heme B was mainly present

285   inside of the veins, while taurocholic acid was present in the PP region (Figure 3Aii, S6A and S5E). On

286   the same region, ten cell-type-specific and tissue structure markers illuminated a heterogeneous cell

287   landscape and recapitulated the anatomical structures in the mouse liver (Figure 3 Aii). The single ion

288   images of selected species are detailed in Figure S6, exhibiting various distribution patterns.

289

290   Principle component analysis (PCA) revealed clusters of ions contributing to the major features around

291   the CV and PV (Figure S7). Heme B, a marker for vasculature, was highly concentrated inside the vein in

292   principal component 2 (PC2). As an exclusive and essential lipid constituent of mitochondrial membranes,

293   a variety of cardiolipins (CLs) was elevated around the PV rather than the CV, which is in line with the

294   oxygen gradient captured in PC4 (Paradies et al., 2014). PC5 highlights the CV region with species

295   PI(38:4), PS(38:4), PA(38:4), LPA(18:0), FA(20:4) and PS(38:3). On the other hand, PC6 shows the

296   radiated gradient around the PV with dominated species LPS(16:1), and LPS(16:0), echoing an earlier

297   study on increased PS-PLA1 or LPS receptor 1 (LPS1) mRNA in hepatocellular carcinoma (HCC)

298   tissues(Uranbileg et al., 2020). The chemical gradients of these species were measured along the porto-

299   central axis by line scanning (Figure 3B). Glucose appeared more abundant inside the CV and PV, the

300   same as Heme B. GSH and AMP had similar patterns as glucose, indicating high energy consumption in

301   the CV and PV region. Most PI species were concentrated around the CV region (e.g., PI(38:4)), while

302   PA and PS species were found to be higher in the PV region (e.g., PA(40:6), PS(40:6)). PE(40:6) appeared

303   to be more intense at the edge of the CV and PV, contributing to the curved structure and mechanical

304   resistance facilitated by the conical shape of PE). Figure S8 demonstrates more species with similar

305   chemical gradients across the CV and PV.

306

307   Sequential C_{60}-SIMS imaging on the same region profiled by $(H_2O)_{n(n=30k)}$-GCIB-SIMS further revealed

308   the distribution of targeted protein markers using a panel of lanthanide-labeled antibodies. The panel was

309 designed to identify major cell types, immune cells, cell boundaries and zonation markers within liver

310 (Table S1). Leukocytes, Ito stellate cells, sinusoidal endothelial cells and macrophages/Kupffer cells were

311 localized with the markers CD45/CD11b red, GFAP in yellow, LYVE-1 in white, CD68 and F4/80 in

312 magenta, respectively (Figure 3Aii). As expected, GS (in Green) expression was abundant around CV,

313 which is consistent with RNAScope results (Figure S2b). EGFR and Na/K-ATPase in cyan defined the

314 cell border, facilitating cell segmentation and image alignment to register multiple lipids and metabolites

315 in individual cells. The single-channel imaging of each antibody using C_{60}-SIMS (Figure S10) was

316 validated by immunohistochemistry (IHC) (Figure S9).

317

318 Image processing for alignment, registration, and cell segmentation by Deepcell(Keren et al., 2018) are

319 described in Figure 3 Aiii and detailed in Figure S15-17. With this, the detected omics molecules using

320 dual- SIMS imaging were registered to individual segmented cells for further statistical analysis. The

321 hierarchical clustering algorithm (HCA) compares the intensities variation of monitored metabolites/lipids

322 among different cell types, providing a comprehensive view of cell signatures and metabolic states. As

323 shown in Figure 3C, GS expressing cells comprise significant PI(38:4), which metabolizes to downstream

324 signaling molecules phosphatidylinositol phosphate (PIPs) known to bind many proteins and control

325 protein-protein interactions(Amos et al., 2019). PE(40:6) also contributes to the GS-positve cells,

326 particularly cells in the inner circle of the CV and PV. Along with PA(38:4), PS(38:4), GD(d40:1),

327 PI(40:6), PE(38:4), PI(40:4), PE(36:2), FA(20:0), PA(41:6) and PI(36:4), these lipids were more abundant

328 in Glul-positive cells around the CV. The glucose content was highest among the CD11b positive cells,

329 suggesting a high glucose-dependant metabolism. Sinusoidal cells labeled by LYVE-1 are rich in lipids

330 with a low degree of unsaturation. Cells expressing the periportal hepatocyte-specific marker

331 (Heppar1/CPS1) consist of a higher level of LPAs and cardiolipins.

332

333 Next, t-distributed stochastic neighbor embedding (t-SNE) was performed to cluster the single cell data

334 points that integrate the omics molecules detected using SIMS, showing metabolites and lipids only can

335 classify the cell populations. As in Figure 3D, Clusters 1-8 highlight the regions around the PP and PC

336 regions, particularly cluster 1, identifying the portal endothelial cells that are consistent with the

337 localization of LYVE-1 positive cells (Figure 3Di, 3Dii). The cells in clusters 2-6 are co-localized with

338 Heppar-1 positive cells (Figure 3 Dii). Separating the same type of cells into distinct clusters is likely

339 related to the vastly different metabolic/lipidomic states of hepatocytes at various locations, and reflects

340   the varying functions among the same cell types. Cluster 7-8 are around the CV, the exact location of Glul

341   expressing cells (Figure 3 Di, 3 Dii). Hence, the abundance of metabolites and lipids allows for clustering

342   of cells into distinct subpopulations, some of which are not captured by conventional protein markers.

343   ***SIMS delineates heterogeneity by cell-type specific multi-omics at single cell level in human liver***

344   The same workflow for dual SIMS imaging was repeated around PT on a human liver tissue section

345   (Figure 4). The high-resolution images demonstrated the heterogeneous biomolecules, as PS (36:1)

346   outlined the PT, PI (38:4) was localized outside the PT primarily, and Heme B was inside of the PT

347   (Figure 4 Aii). The single ion images of 246 metabolites and lipids are in Figure S11, among them, 120

348   species were annotated.

349

350   PCA analysis distinguished two anatomical features and metabolic flux around the PT (Figure S12). The

351   PT ring has abundant PS(36:1), PA(36:1) and PI(38:4), with significant higher PS(36:1) that defines the

352   PT region. Inside the PT ring, Heme B and several PA species are dominant. The metabolic flux also

353   shows anti-correlated patterns, with taurodeoxycholic acid/taurodeoxycholic, FA (C18:2) and FA (C18:1),

354   taurocholic acid and PEp(40:6) to the left of the PT ring and GSH to the right.

355

356   On the same tissue, protein markers show the major cell types, immune cells and cell states (Figure 4

357   Aiii). With the same computational process (Figure 3 Aiii), HCA elucidates the variation of monitored

358   metabolites/lipids in different cell types and structural regions , namely CD4, CD45, Epcam, LYVE-1,

359   CD68, SMA and collagen I (Figure 4B). IHC validation and single-channel image of antibody panel

360   (Table S2) are detailed in Figure S13 and S14, respectively. T-helper cells (CD4) and leukocytes (CD45),

361   were located mainly around the PT, sharing similar metabolism of high glucose consumption. Epcam, as

362   an epithelial antigen, shows the highest GSH level that correlates to the activation of antioxidant

363   mechanism. Sinusoidal cells (LYVE-1) comprise the higher ganglioside GM3 and PE species, which are

364   highly relevant to cell adherence and mechanical resistance to highly packed cellular region (Calzada et

365   al., 2016; Labrada et al., 2018). Without distinct lipidomic and metabolic features, macrophage/Kupffer

366   cells (CD68) seemed to have slightly higher CLs, representing a higher number of mitochondria. As a

367   major tissue structure marker, SMA is co-localized with PS 36:1 abundant region.

368

369   tSNE clustering was further applied to classify cells using metabolites and lipids (Figure 4 Ci and 4 Cii).

370   Cluster 1, 4, 5 and 8 were consistent with the GFAP, collagen I, CD45 and SMA positive cells,

371   respectively. Low expression of Arg-1, CD4, Glul and CK19 were also observed in these clusters.

372   Periportal hepatocytes expressing Arg-1 and Albumin were sub-classified into clusters 2, 3, 6 and 7. The

373   overlapping of protein markers for each tSNE cluster was likely to be the shared signature metabolites

374   and lipids among them. Several factors contributed to the success of the cell classification by metabolites

375   and lipids, the successive high-resolution SIMS images on the same tissue that facilitates the accurate cell

376   segmentation and image registration, and cryogenic SIMS workflow that preserves the pristine chemistry

377   in single cells.

378

379   ***RNAScope, MALDI Orbitrap and LC-MS to validate the core MSI workflow***

380   To validate antibody markers used in the study, namely CD68, Glul, Albumin and LYVE1, single-

381   molecule mRNA fluorescent *in situ* hybridization was performed on human liver tissue section. Color

382   overlaid images of RNAScope show the distribution of the RNA copies (Figure S4) consistent with images

383   of proteins (Figure S9, S10, S13 and S14). For example, protein GS and its corresponding mRNA

384   transcript, *Glul*, were localized around CV, but not PV. In addition, fluorescent slide scanning allowed

385   easy identification of PV and CV, compared to H&E staining in mouse liver tissue sample (Figure S1b).

386

387   The identity of the zone-specific lipids was assessed using accurate mass match of the MSI-derived ions

388   of interest against the library databases(Fahy et al., 2009) followed by UPLC-MS^E fragment analysis from

389   lipidomics analysis from liver tissue lipid extracts (Table 1). The analysis of DESI and lipidomics analysis

390   with lockmass correction helps to align the precursor mass with high accuracy. The UPLC-MS^E data was

391   searched for the most commonly formed adducts, [M+ H$^+$, Na$^+$, K$^+$]$^+$ in positive ion mode for DESI and

392   [M-H]$^-$ for negative ion mode for both DESI and SIMS. The metabolites were annotated by accurate mass

393   search against the library database(Smith et al., 2005; Wishart et al., 2022) and accurate mass and ion

394   mobility drift time of the standard when available. Most of the precursor ion matches between the DESI

395   and LC-MS were phospholipids and glycerolipids in positive ion mode, and for SIMS were phospholipids

396   in negative ion mode. Similarly, confirmation of lipid species based on MALDI is shown in Table S3 and

397   S4. DESI and SIMS identified a complementary list of species around CV and PV (Table 1), resulting

398   from the difference in preferential ionization for different lipid species. High-resolution SIMS uncovered

399   several metabolites and lipids that have a thin circulate structure around both central and portal veins, such

400   as GSH, AMP, PE(40:6), PA(36:1), PS(38:3) and PI(38:4); some species were much more concentrated

401   inside the veins, such as LPAs (Figure S6 and Figure S11). While DESI confirmed distinct distributions

402   of more free fatty acids, conjugated bile acids and glycerolipids (Figure 2 and Figure S3). All species were

403   validated by in situ tandem MS using MALDI (Table S3 and S4). However, metabolites and fatty acids

404   are not validated by MALDI due to the mass interferences for species below *m/z* 350 from the matrix. The

405   results demonstrate the complementary approach using a variety of MSI methods for more comprehensive

406   imaging of biosamples.

407

408   **Discussion**

409   This study demonstrates for the first time major technological improvements that enable a multi-modal

410   workflow for multiplexed imaging of metabolites, lipids and proteins for integrated spatial omics at

411   anatomical structure and single-cell resolution. The multi-scale biomolecule detection works efficiently

412   to distinguish anatomical features (*e.g.,* CV, PV and PT) and metabolic zones in liver tissue. Moreover,

413   significant variations of species are observed in different types of liver cells (*e.g*., hepatocytes, Kupffer,

414   sinusoidal cells, macrophages, T cells and leucocytes), demonstrating that different metabolic states are

415   needed for spatial division of labor to efficiently manage a multitude of metabolic functions. Finally, we

416   observed sex-specific differences in the distributions of many lipid species, suggesting that male and

417   female livers may be functionally quite distinct, with implications for understanding sex-specific

418   differences in disease risk.

419

420   There is growing interest in dissecting cellular and metabolic heterogeneity directly on tissue at single-

421   cell resolution. Spatial metabolomics is becoming an attractive approach to answer questions about liver

422   metabolic reprogramming, which is associated with a spectrum of liver diseases. This requires

423   characterizing cell types and cell neighborhoods, as well as an atlas of biomolecule abundances within the

424   cell types, taking into account where these cell types exist within the tissue architecture. However, there

425   are few analytical tools to image multiple types of molecules in single cells directly on tissue without

426   dissociation. Consecutive SIMS imaging on the same frozen-hydrated tissue offers single-cell resolution

427   and high chemical sensitivity to integrate spatial multi-omics (untargeted metabolomics and lipidomics

428   and targeted proteomics) in the same individual cells and at a near-native state of biological tissue. With

429   well-preserved gradients of small molecules, which would be otherwise diffused by any chemical fixation

430   and drying process, the metabolic state of different types of cells can be revealed in liver tissue. In addition,

431   cell population separation on tissue directly by metabolic states has not been reported, but some success

432   has been shown on classification of co-cultured cells by metabolic states using MALDI imaging and

433   computational approach SpaceM(Rappez et al., 2021).

434

435   With cryogenic multi-modal SIMS imaging at high-resolution and data processing, we show for the first

436   time that integrated metabolomic and lipidomic profiling in individual cells can be used for cell

437   classifications without protein markers and tissue dissociation. Additionally, subsets of cell types are

438   captured by distinct metabolic signatures among cells expressing the same proteins. As the role of

439   individual lipid species are understudied, this platform could be extended to overlay spatial

440   transcriptomics and proteomics characterizing the distribution of enzymes involved in lipid metabolism

441   to fully elucidate the spatial diversity and its functional significance. This will provide a rare opportunity

442   to investigate previously unknown cellular subtypes and their unique protein-lipid-metabolite interactions.

443

444   A robust pipeline with high-resolution multi-modal MSI and computational processing adds layers of

445   spatial omics about metabolic and lipidomic heterogeneity in different types of cell populations,

446   distinguishing subpopulations and distinct metabolic functions within individual cells on normal liver

447   tissue. This workflow can be readily applied to liver disease models for the discovery of metabolic

448   vulnerability and associated cell types, heterogenous shift of disease microenvironment, and cell-to-cell

449   interaction, ultimately leading to new therapeutic opportunities.

450

451   **References**

452   Aizarani, N., Saviano, A., Sagar, Mailly, L., Durand, S., Herman, J.S., Pessaux, P., Baumert, T.F., and

453   Grun, D. (2019). A human liver cell atlas reveals heterogeneity and epithelial progenitors. Nature *572*,

454   199-204.

455   Alexandrov, T., Becker, M., Deininger, S.O., Ernst, G., Wehder, L., Grasmair, M., von Eggeling, F.,

456   Thiele, H., and Maass, P. (2010). Spatial segmentation of imaging mass spectrometry data with edge-

457   preserving image denoising and clustering. J Proteome Res *9*, 6535-6546.

458   Amigo, L., Mendoza, H., Zanlungo, S., Miquel, J.F., Rigotti, A., Gonzalez, S., and Nervi, F. (1999).

459   Enrichment of canalicular membrane with cholesterol and sphingomyelin prevents bile salt-induced

460   hepatic damage. J Lipid Res *40*, 533-542.

461 Amos, S.-B.T.A., Kalli, A.C., Shi, J., and Sansom, M.S.P. (2019). Membrane Recognition and Binding
462 by the Phosphatidylinositol Phosphate Kinase PIP5K1A: A Multiscale Simulation Study. Structure
463 (London, England : 1993) *27*, 1336-1346.e1332.

464 Bannon, D., Moen, E., Schwartz, M., Borba, E., Kudo, T., Greenwald, N., Vijayakumar, V., Chang, B.,
465 Pao, E., Osterman, E.*, et al.* (2021). DeepCell Kiosk: scaling deep learning-enabled cellular image
466 analysis with Kubernetes. Nat Methods *18*, 43-45.

467 Beare, R., Lowekamp, B., and Yaniv, Z. (2018). Image Segmentation, Registration and Characterization
468 in R with SimpleITK. J Stat Softw *86*.

469 Borner, K., Teichmann, S.A., Quardokus, E.M., Gee, J.C., Browne, K., Osumi-Sutherland, D., Herr,
470 B.W., 2nd, Bueckle, A., Paul, H., Haniffa, M.*, et al.* (2021). Anatomical structures, cell types and
471 biomarkers of the Human Reference Atlas. Nat Cell Biol *23*, 1117-1128.

472 Bradley, A.P. (1997). The use of the area under the roc curve in the evaluation of machine learning
473 algorithms. Pattern Recogn *30*, 1145-1159.

474 Calzada, E., Onguka, O., and Claypool, S.M. (2016). Phosphatidylethanolamine Metabolism in Health
475 and Disease. Int Rev Cell Mol Biol *321*, 29-88.

476 Caprioli, R.M., Farmer, T.B., and Gile, J. (1997). Molecular imaging of biological samples: localization
477 of peptides and proteins using MALDI-TOF MS. Anal Chem *69*, 4751-4760.

478 Djambazova, K.V., Klein, D.R., Migas, L.G., Neumann, E.K., Rivera, E.S., Van de Plas, R., Caprioli,
479 R.M., and Spraggins, J.M. (2020). Resolving the Complexity of Spatial Lipidomics Using MALDI
480 TIMS Imaging Mass Spectrometry. Anal Chem *92*, 13290-13297.

481 Eberlin, L.S. (2014). DESI-MS imaging of lipids and metabolites from biological samples. Methods Mol
482 Biol *1198*, 299-311.

483 El-Achkar, T.M., Eadon, M.T., Menon, R., Lake, B.B., Sigdel, T.K., Alexandrov, T., Parikh, S., Zhang,
484 G., Dobi, D., Dunn, K.W.*, et al.* (2021). A multimodal and integrated approach to interrogate human
485 kidney biopsies with rigor and reproducibility: guidelines from the Kidney Precision Medicine Project.
486 Physiol Genomics *53*, 1-11.

487 Fahy, E., Subramaniam, S., Murphy, R.C., Nishijima, M., Raetz, C.R., Shimizu, T., Spener, F., van
488 Meer, G., Wakelam, M.J., and Dennis, E.A. (2009). Update of the LIPID MAPS comprehensive
489 classification system for lipids. J Lipid Res *50 Suppl*, S9-14.

490 Gebhardt, R., and Matz-Soja, M. (2014). Liver zonation: Novel aspects of its regulation and its impact
491 on homeostasis. World J Gastroenterol *20*, 8491-8504.

492   Geisler, C.E., and Renquist, B.J. (2017). Hepatic lipid accumulation: cause and consequence of

493   dysregulated glucoregulatory hormones. J Endocrinol *234*, R1-R21.

494   Guzman, M., and Castro, J. (1989). Zonation of fatty acid metabolism in rat liver. Biochem J *264*, 107-

495   113.

496   Halpern, K.B., Shenhav, R., Matcovitch-Natan, O., Toth, B., Lemze, D., Golan, M., Massasa, E.E.,

497   Baydatch, S., Landen, S., Moor, A.E.*, et al.* (2017). Single-cell spatial reconstruction reveals global

498   division of labour in the mammalian liver. Nature *542*, 352-356.

499   Hickey, J.W., Neumann, E.K., Radtke, A.J., Camarillo, J.M., Beuschel, R.T., Albanese, A.,

500   McDonough, E., Hatler, J., Wiblin, A.E., Fisher, J.*, et al.* (2022). Spatial mapping of protein

501   composition and tissue organization: a primer for multiplexed antibody-based imaging. Nat Methods *19*,

502   284-295.

503   Hu, B.C. (2019). The human body at cellular resolution: the NIH Human Biomolecular Atlas Program.

504   Nature *574*, 187-192.

505   Ikeda, S., Tachikawa, M., Akanuma, S., Fujinawa, J., and Hosoya, K. (2012). Involvement of gamma-

506   aminobutyric acid transporter 2 in the hepatic uptake of taurine in rats. Am J Physiol Gastrointest Liver

507   Physiol *303*, G291-297.

508   Keren, L., Bosse, M., Marquez, D., Angoshtari, R., Jain, S., Varma, S., Yang, S.R., Kurian, A., Van

509   Valen, D., West, R.*, et al.* (2018). A Structured Tumor-Immune Microenvironment in Triple Negative

510   Breast Cancer Revealed by Multiplexed Ion Beam Imaging. Cell *174*, 1373-1387 e1319.

511   Kessner, D., Chambers, M., Burke, R., Agus, D., and Mallick, P. (2008). ProteoWizard: open source

512   software for rapid proteomics tools development. Bioinformatics *24*, 2534-2536.

513   Kietzmann, T. (2017). Metabolic zonation of the liver: The oxygen gradient revisited. Redox Biol *11*,

514   622-630.

515   Labrada, M., Dorvignit, D., Hevia, G., Rodríguez-Zhurbenko, N., Hernández, A.M., Vázquez, A.M., and

516   Fernández, L.E. (2018). GM3(Neu5Gc) ganglioside: an evolution fixed neoantigen for cancer

517   immunotherapy. Semin Oncol *45*, 41-51.

518   Lamers, W.H., Hilberts, A., Furt, E., Smith, J., Jonges, G.N., van Noorden, C.J., Janzen, J.W., Charles,

519   R., and Moorman, A.F. (1989). Hepatic enzymic zonation: a reevaluation of the concept of the liver

520   acinus. Hepatology *10*, 72-76.

521   Longo, N., Frigeni, M., and Pasquali, M. (2016). Carnitine transport and fatty acid oxidation. Biochim

522   Biophys Acta *1863*, 2422-2435.

523   Mandrekar, J.N. (2010). Receiver operating characteristic curve in diagnostic test assessment. J Thorac
524   Oncol *5*, 1315-1316.

525   Mittendorfer, B. (2005). Sexual dimorphism in human lipid metabolism. J Nutr *135*, 681-686.

526   Paradies, G., Paradies, V., De Benedictis, V., Ruggiero, F.M., and Petrosillo, G. (2014). Functional role
527   of cardiolipin in mitochondrial bioenergetics. Biochim Biophys Acta *1837*, 408-417.

528   Quistorff, B., Katz, N., and Witters, L.A. (1992). Hepatocyte heterogeneity in the metabolism of fatty
529   acids: discrepancies on zonation of acetyl-CoA carboxylase. Enzyme *46*, 59-71.

530   Race, A.M., Styles, I.B., and Bunch, J. (2012). Inclusive sharing of mass spectrometry imaging data
531   requires a converter for all. J Proteomics *75*, 5111-5112.

532   Radtke, A.J., Kandov, E., Lowekamp, B., Speranza, E., Chu, C.J., Gola, A., Thakur, N., Shih, R., Yao,
533   L., Yaniv, Z.R.*, et al.* (2020). IBEX: A versatile multiplex optical imaging approach for deep
534   phenotyping and spatial analysis of cells in complex tissues. Proc Natl Acad Sci U S A *117*, 33455-
535   33465.

536   Rappez, L., Stadler, M., Triana, S., Gathungu, R.M., Ovchinnikova, K., Phapale, P., Heikenwalder, M.,
537   and Alexandrov, T. (2021). SpaceM reveals metabolic states of single cells. Nat Methods *18*, 799-805.

538   Rozenblatt-Rosen, O., Regev, A., Oberdoerffer, P., Nawy, T., Hupalowska, A., Rood, J.E., Ashenberg,
539   O., Cerami, E., Coffey, R.J., Demir, E.*, et al.* (2020). The Human Tumor Atlas Network: Charting
540   Tumor Transitions across Space and Time at Single-Cell Resolution. Cell *181*, 236-249.

541   Sheraz, S., Tian, H., Vickerman, J.C., Blenkinsopp, P., Winograd, N., and Cumpson, P. (2019).
542   Enhanced Ion Yields Using High Energy Water Cluster Beams for Secondary Ion Mass Spectrometry
543   Analysis and Imaging. Anal Chem *91*, 9058-9068.

544   Simons, K., and Ehehalt, R. (2002). Cholesterol, lipid rafts, and disease. J Clin Invest *110*, 597-603.

545   Sirma, H., Williams, G.M., and Gebhardt, R. (1996). Strain- and sex-specific variations in hepatic
546   glutamine synthetase activity and distribution in rats and mice. Liver *16*, 166-173.

547   Smith, C.A., O'Maille, G., Want, E.J., Qin, C., Trauger, S.A., Brandon, T.R., Custodio, D.E., Abagyan,
548   R., and Siuzdak, G. (2005). METLIN: a metabolite mass spectral database. Ther Drug Monit *27*, 747-
549   751.

550   Soares, A.F., Paz-Montoya, J., Lei, H., Moniatte, M., and Gruetter, R. (2017). Sexual dimorphism in
551   hepatic lipids is associated with the evolution of metabolic status in mice. NMR Biomed *30*.

552 Sud, M., Fahy, E., Cotter, D., Brown, A., Dennis, E.A., Glass, C.K., Merrill, A.H., Jr., Murphy, R.C.,

553 Raetz, C.R., Russell, D.W.*, et al.* (2007). LMSD: LIPID MAPS structure database. Nucleic Acids Res

554 *35*, D527-532.

555 Takats, Z., Wiseman, J.M., and Cooks, R.G. (2005). Ambient mass spectrometry using desorption

556 electrospray ionization (DESI): instrumentation, mechanisms and applications in forensics, chemistry,

557 and biology. J Mass Spectrom *40*, 1261-1275.

558 Taylor, M.J., Lukowski, J.K., and Anderton, C.R. (2021). Spatially Resolved Mass Spectrometry at the

559 Single Cell: Recent Innovations in Proteomics and Metabolomics. J Am Soc Mass Spectrom *32*, 872-

560 894.

561 Tian, H., Sheraz Nee Rabbani, S., Vickerman, J.C., and Winograd, N. (2021). Multiomics Imaging

562 Using High-Energy Water Gas Cluster Ion Beam Secondary Ion Mass Spectrometry [(H2O)n-GCIB-

563 SIMS] of Frozen-Hydrated Cells and Tissue. Anal Chem *93*, 7808-7814.

564 Tian, H., Sparvero, L.J., Blenkinsopp, P., Amoscato, A.A., Watkins, S.C., Bayır, H., Kagan, V.E., and

565 Winograd, N. (2019). Secondary-Ion Mass Spectrometry Images Cardiolipins and

566 Phosphatidylethanolamines at the Subcellular Level. Angew Chem Int Ed Engl *58*, 3156-3161.

567 Trefts, E., Gannon, M., and Wasserman, D.H. (2017). The liver. Curr Biol *27*, R1147-R1151.

568 Uranbileg, B., Kurano, M., Sato, M., Ikeda, H., Ishizawa, T., Hasegawa, K., Kokudo, N., and Yatomi,

569 Y. (2020). Possible involvement of PS-PLA1 and lysophosphatidylserine receptor (LPS1) in

570 hepatocellular carcinoma. Sci Rep-Uk *10*.

571 Wang, F., Flanagan, J., Su, N., Wang, L.C., Bui, S., Nielson, A., Wu, X., Vo, H.T., Ma, X.J., and Luo,

572 Y. (2012). RNAscope: a novel in situ RNA analysis platform for formalin-fixed, paraffin-embedded

573 tissues. J Mol Diagn *14*, 22-29.

574 Winograd, N. (2018). Gas Cluster Ion Beams for Secondary Ion Mass Spectrometry. Annu Rev Anal

575 Chem (Palo Alto Calif) *11*, 29-48.

576 Wishart, D.S., Guo, A., Oler, E., Wang, F., Anjum, A., Peters, H., Dizon, R., Sayeeda, Z., Tian, S., Lee,

577 B.L.*, et al.* (2022). HMDB 5.0: the Human Metabolome Database for 2022. Nucleic Acids Res *50*,

578 D622-D631.

579

580 Acknowledgments

583 like to show our gratitude to Dr. Dan Graham from the University of Washington and Dr. Nathan H.

584 Patterson from Vanderbilt University for sharing their expertise in MSI data processing.

585

586 **Author contributions**

587 HT, PR and BRS designed the multimodal imaging workflow for liver tissue study. HT conceived the

588 dual-SIMS imaging workflow, established the lanthanide-conjugated antibody panel and immunostaining

589 protocol, and performed tissue immunostaining, SIMS data acquisition and general/discriminant

590 processing. PR optimized sample processing for multimodal imaging, performed sample preparation,

591 DESI imaging and data analysis, lipidomic experiment and data analysis and multimodal data comparison.

592 JT developed the software platform and algorithm for data processing, image registration and

593 segmentation under the supervision of HT. AMD performed RNAScope imaging and analysis. TVN

594 performed cryosectioning and assessed IHC data with PR. TA performed MALDI imaging. FZ contributed

595 to lipidomic experiments. TVN and JD performed mouse tissue sample preparation. HR performed tissue

596 identification, pathological analysis and annotation of tissue structure. NW provided the SIMS

597 instrumentation. HT, PR and BRS drafted and edited the paper. BRS supervised the project. HT and PR

598 contributed equally.

599

600 **Declaration of interests**

601 B.R.S. is an inventor on patents and patent applications involving small molecule drug discovery,

602 ferroptosis, and immunostaining, co-founded and serves as a consultant to Inzen Therapeutics, Exarta

603 Therapeutics, and ProJenX Inc, and serves as a consultant to Weatherwax Biotechnologies Corporation

604 and Akin Gump Strauss Hauer & Feld LLP. All other authors declare no competing financial interests.

605

606

607

608

609

610

611

612

613

614

615

616

617 **Figure Legends**

618 Figure 1. Schematics of MSI-centric multimodal imaging workflow reveals 2D/3D biomolecular atlas of

619 human liver. Consecutive sections from liver tissue blocks are assessed by A, DESI-MSI exhibiting the

620 distribution of lipids and metabolites within histologically defined structural units of liver within the tissue

621 architecture and B, SIMS-MSI including $(H_2O)_n$-GCIB-SIMS for lipid and metabolite imaging at single

622 cell resolution followed by C60-SIMS on the same tissue section, followed by image integration and single

623 cell specific lipid and metabolite extraction C, Validation of lipids detected by DESI and SIMS and D,

624 structural elucidation by UPLC-MSE lipidomics on liver tissue section homogenate E, The 2D images

625 from DESI and SIMS are aligned for 3D reconstruction and visualization.

626

627 Figure 2. DESI MSI reveals periportal and pericentral specific lipids and metabolites in mouse and human

628 liver. Ai, H&E staining performed on a normal mouse liver section to identify the central vein (CV) and

629 portal triad (PT) regions. Aii, RNAScope is performed on a consecutive tissue section stained for

630 expression of Albumin (Alb-yellow) and Glutamine Synthetase (Glul- magenta) showing differential

631 staining for periportal (PP) and pericentral (PC) regions respectively. Aiii, Av, Spatial segmentation of

632 pixels based on distribution of a few lipids and metabolites from DESI-MSI in (Aiii) negative and (Av)

633 positive ion mode. (Aiv, Avi) Distribution of a few lipids and metabolites showing PC and PP specificity

634 in both ion modes are shown. B, Heatmap depicting the predictive performance of features measured by

635 AUC-ROC (in rows) and classification (in columns) from DESI for PP and PC regions in female (n=3)

636 and male (n=3) mice liver sections. C, Fold change values comparing the mean intensity of PC versus PP

637 regions for the features from (B) Error bars represent mean ± standard deviation. D, H&E section with

638 manual annotation of CV and PT regions in human liver section. The corresponding images for

639 distribution of different classes of lipids are shown. E, Distribution of lipids in consecutive sections for 3-

640 dimensional visualization of lipids as shown in Supp video1.

641

642 Figure 3 Dual high-resolution SIMS imaging delineates the metabolomic and lipidomic states in different

643 cell types on the mouse liver section. Ai, H&E staining image of central vein (CV) and portal vein (PV)

644 region. Aii, Representative color overlay images of Dual-SIMS. Metabolites and lipids image in the same

645 region as in Ai on a serial frozen-hydrated section using $(H_2O)_{n(n=30k)}$-GCIB-SIMS at the spatial resolution

646 of 3 µm, Blue, PI 38:4; Magenta, Taurocholic acid ; Yellow, PS 40:6; Green, HEME B. More single specie

647 images are in Figure S6. Proteins image by lanthanides-conjugated antibodies from the region highlighted

648 in the red box using C_{60}-SIMS at the spatial resolution of 1 µm, Red, CD45 and CD11b; Yellow, GFAP;

649 White, LYVE-1; Magenta, F4/80 and CD68; Cyan, EGFR and Na/KATPase; Green, Glul; Blue, Nuclei.

650 Scale bar 100 µm. Aiii, Registration of dual-SIMS images for alignment; Single cell segmentation using

651 DeepCell. More details are described in supplementary Figures S16 and S17. B, Intensities changes of

652 various species from the center of CV to PV (as the blue line in A i). C, HCA map shows the variation of

653 different metabolites/lipids in various types of cells. Di, tSNE clustering to classify the cell types as in

654 cluster 1-8 by lipids and metabolites only. Dii, Correlation of cluster 1-8 to 9 protein markers.

655

656 Figure 4. Dual high-resolution SIMS imaging delineates the metabolomic and lipidomic states in different

657 cell types on the human liver tissue section. Ai, H&E image. The selected region contains the central vein

658 and portal vein. Aii, Representative color overlay images of Dual-SIMS. Metabolites and lipids image in

659 the same region as in Ai on a serial frozen-hydrated section using $(H_2O)_{n(n=30k)}$-GCIB-SIMS at the spatial

660 resolution of 3 µm, Blue, PS 36:1; Magenta, PI 38:4; Green, HEME B. More single specie images are in

661 Figure S10. Proteins image by lanthanides-conjugated antibodies from the same region after $(H_2O)_{n(n=30k)}$-

662 GCIB-SIMS using C_{60}-SIMS at spatial resolution of 1 µm, Red, CD45 and CD11b; Magenta, GFAP;

663 White, LYVE-1; Yellow, Heppar-1; Cyan, EGFR and Na/KATPase; Green, Glul; Blue, Nuclei. Aiii, The

664 image alignment and registration of dual-SIMS images (i.e., Aii and Aiii). More details are described in

665 supplementary Figures S16 and S17. B, HCA map shows the variation of different metabolites/lipids in

666 different types of cells. Ci, tSNE clustering to classify the cell types as in cluster 1-8 by lipids and

667 metabolites only. Cii, Correlation of cluster 1-8 to 15 protein markers.

668

669

670

671

672

673

674

675

Table 1. Validation of lipid ion species from SIMS and DESI-MSI with MALDI-MSI and LC-MS/MS

Pericentral vein region					Periportal vein region				
$(H_2O)_n$-GCIB-SIMS negative ion mode		MALDI Orbitrap validation	LC-MS precursor mass	LC-MS/MS validation	$(H_2O)_n$-GCIB-SIMS negative ion mode		MALDI Orbitrap validation	LC-MS precursor mass	LC-MS/MS validation
303.23	FA C20:4	NA	NA	NA	255.23	FA C16:0	NA	NA	NA
311.23	FA C20:0	NA	NA	NA	279.23	FA C18:2	NA	NA	NA
742.53	PE 36:2	PE(18:0/18:2)	NA	NA	283.26	FA C18:0	NA	NA	NA
766.54	PE 38:4	PE(18:0/20:4)	NA	NA	514.28	Taurocholic acid	NA	NA	NA
911.56	PI 40:5	PI(18:0/22:5)	NA	NA	747.50	PA 40:6	PA(18:0/22:6)	747.48	PA 40:6
913.58	PI 40:4	PI 40:4	NA	NA	834.53	PS 40:6	PS(18:0/22:6)	834.53	PS 40:6
857.51	PI 36:4	PI(16:0/20:4)	NA	NA	835.53	PI 34:1	PI(12:0/22:1(11Z))	835.53	PI 34:1
723.50	PA 38:4	PA(18:0/20:4)	723.48	PA 18:2/20:2	1454.03	CL 72:5	NA	NA	NA
810.53	PS 38:4	PS(18:0/20:4)	810.54	PS 38:4	1455.95	CL 72:4	NA	NA	NA
812.54	PS 38:3	NA	812.55	PS 38:3	1480.94	CL 74:6	NA	NA	NA
885.55	PI 38:4	PI(18:0/20:4)	885.55	PI 38:4	1482.08	CL 74:5	NA	NA	NA
					1483.94	CL 74:4	NA	NA	NA
					1484.98	CL 74:4	NA		
DESI negative ion mode		MALDI Orbitrap validation	LC-MS precursor mass	LC-MS/MS validation	DESI negative ion mode		MALDI Orbitrap validation	LC-MS precursor mass	LC-MS/MS validation
281.24	FA 18:1	NA	NA	NA	124.01	Taurine	NA	NA	NA
295.23	FA 18:2;O	NA	NA	NA	306.08	GSH	NA	NA	NA
293.21	FA 18:3;O	NA	NA	NA	762.51	PE 38:6	NA	762.50	PE 38:6
309.28	FA 20:1	NA	NA	NA	346.05	AMP/dGMP	NA	NA	NA
311.3	FA 20:0	NA	NA	NA	175.03	Ascorbic acid	NA	NA	NA
307.26	FA 20:2	NA	NA	NA	514.28	ST 24:1;O5;T	NA	NA	NA
					512.27	Sulfoglycolithocholate	NA	NA	NA
					498.29	ST 24:1;O4;T	NA	NA	NA
					790.53	PE 40:6	PE(18:0/22:6)	790.53	PE 40:6
DESI positive ion mode		MALDI Orbitrap validation	LC-MS precursor mass	LC-MS/MS validation	DESI positive ion mode		MALDI Orbitrap validation	LC-MS precursor mass	LC-MS/MS validation
647.46	DG 37:7	NA	647.45	DG 37:7	818.50	PC 36:5	PC 36:5	NA	NA
840.55	PC 39:7	NA	840.55	PC 39:7	756.54	PC 32:0	PC 34:3	756.54	PC 32:0
848.54	PC 38:4	PC 38:4	848.55	PC 38:4	560.31	LPC 18:1	NA	NA	NA
633.48	DG 34:1	NA	633.48	DG 34:1	562.32	LPC 18:0	PC 18:0	NA	NA
631.46	DG 34:2	NA	631.46	DG 34:2	518.32	LPC 16:0	PC 16:0	NA	NA
659.49	DG 36:2	NA	659.49	DG 36:2	760.58	PC 34:1	PC 34:1	NA	NA
657.48	DG 36:3	NA	657.48	DG 36:3	806.56	PC 38:6	PC 36:3	NA	NA
655.46	DG 36:4	NA	655.46	DG 36:4	542.32	LPC 18:2	NA	NA	NA
856.56	PC P-40:6	NA	856.55	PC P-40:6	786.59	PC 36:2	PE(36:2)	786.59	PC 36:2

STAR Methods

RESOURCE AVAILABILITY

Lead contact
Further information and requests for resources and reagents should be directed to and will be fulfilled by the lead contact, Hua Tian: hut3@psu.edu.

Materials availability
This study did not generate new unique reagents.

Data and code availability
- **Data availability**

Mass spectrometry imaging date are in standardized imzML format. SIMS data is available at doi:10.26207/6a38-tr35. DESI and SIMS data will also be available from https://portal.hubmapconsortium.org by end of July 2022. The software license is provided for analyzing the data using Ionoptika Analyser for up to 7 days. Please contact Ionoptika if you wish to use the software beyond 7 days via our Support e-mail (support@ionoptika.co.uk). Accession numbers are listed in the key resources table.

- Any additional information required to reanalyze the data reported in this paper is available from the lead contact upon request.

METHOD DETAILS

Tissue preparation. Normal human liver sample from a 51-year-old female was retrieved from the Columbia University tissue bank, under a protocol approved by the Institutional Review Board and stored at -80°C until use. Mouse liver tissues were derived from 17 weeks old male (n=3) and female (n=3) C57/BL6 mice. The excised liver tissues were flash frozen on dry ice filled with hexane, and stored at -80°C until use. Small blocks of both human and mouse tissue were cryosectioned at 8-10µm thickness and thaw mounted on microscope glass slides for H&E, DESI and RNAScope analysis and gold-coated slides for SIMS analysis. For multimodal imaging, consecutive sections for DESI, H&E, SIMS and RNAScope were placed on the respective slides and stored at -80°C until analysis.

* Corresponding authors: Hua Tian: hut3@psu.edu; Brent R. Stockwell: bstockwell@columbia.edu
# These authors contributed equally to this work
Lead contact for resource requirement: hut3@psu.edu

Histology. Tissue sections were stained with hematoxylin and eosin (H&E) staining at Columbia University Molecular Pathology Shared Resource facility, scanned at 20X magnification and histological examination was performed by a pathologist to annotate the anatomical structures.

DESI MSI data acquisition and analysis. All the experiments were performed on Synapt G2-Si QToF mass spectrometer (Waters, Milford, MA), coupled to a DESI ion source. Data was acquired in sensitivity mode in both positive and negative ion mode. The DESI parameters used were capillary voltage and sampling cone voltage of 0.65kV and 50V respectively, scan time of 0.145 sec/pixel, pixel size of 40 µm^2, DESI sprayer angle of 75°, nebulizing gas (N$_2$) pressure of 0.3 PSLM. The solvent used was methanol: water 95:5 (v/v) with 0.01% formic acid and 20pg/µl leucine enkephalin, at a flow rate of 1.5 µl/min. Tissue sections were dried in a desiccator for ~10 min prior to analysis. Peak picking and lockmass correction using the protonated ion of leucine enkephalin ([M+H]$^+$, m/z 556.2771) or the deprotonated molecular ion ([M-H]$^-$, m/z 554.2615) was implemented in MassLynx software (Waters, version 4.1). The centroided data files were converted to mzml using msconvert from Proteowizard(Kessner et al., 2008) followed by conversion to imzml format using imzMLConverter(Race et al., 2012). The imzml files were imported into the SCiLS lab software (Bruker, version 2021c) and subsequent data analysis was performed. Total ion count (TIC) normalization was performed and up to n peaks were selected of m/z intervals of ±0.03Da were selected. Spatial segmentation analysis was performed using bisecting k-means clustering on edge-preserving denoised data. Area under the receiver operator characteristic curve was also performed within the SCiLS platform.

Untargeted Lipidomics sample preparation. 20 mg of liver was homogenized using beadrupter and lipids were extracted using 1050ul of 1:2 ratio of ice-cold methanol containing 0.01% w/v butylated hydroxyl toluene and dichloromethane, vortex mixing and incubating the samples overnight at -20C. One volume of ice-cold water was added and mixed for phase separation followed by centrifugation. The lower organic phase containing lipids were collected in a new vial, dried under a gentle stream of nitrogen and stored at -80C until analysis. The samples were reconstituted in isopropanol: acetonitrile: water at the ratio of 11:9:2 v/v/v before analysis.

Chromatographic separation and mass spectrometry analysis. Lipidomics experiments were performed on Synapt G2-Si mass spectrometer equipped with Acquity UPLC system (Waters, Milford,

750   MA) in both positive and negative electrospray ion modes. The chromatographic separation was

751   performed on Acquity UPLC BEH300 C18 column (1.7um particle size, 2.1X100mm) (Waters, Milford,

752   MA) over an 18 min gradient. The column temperature was set at 55C. A binary mobile phase consisted

753   of (A) 60:40 v/v acetonitrile: water and (B) 85:10:5 v/v/v isopropanol/acetonitirile/water, each containing

754   10mM ammonium acetate and 0.1% acetic acid. The gradient was initiated at 40% B, followed by linear

755   gradient to 50% by 2min ramped up to 99%B by 18min, and the column was equilibrated for 2min to the

756   initial condition. The flow rate was set at 400ul/min and injection volume was 2ul in positive mode and

757   5ul in negative mode. Data was acquired on high-definition data independent mode with ion mobility

758   (HDMS^E), over the mass range of m/z 50 to 1200 Da and scan rate of 0.1sec per scan. The parameters

759   used for mass spectrometry data acquisition is as follows: for positive and negative mode, capillary voltage

760   and sampling cone voltage of 2.8kV and 35V; and 2.5kV and 32V were used respectively. The source and

761   desolvation temperature were 120°C and 500°C respectively. Desolvation gas (N$_2$) flow was set at 850

762   L/hr. MS data was calibrated using leucine encephalin infusion at a flow rate of 10µl/min. Default ion

763   mobility settings were used. The low collision energy was set at 4 eV and high energy was 25-60 eV.

764   Mass calibration was performed using sodium formate and collision cross section (CCS) calibration was

765   performed using CCS Major mix (Waters).

766

767   **Lipid and metabolite identification.** The assignment of lipids and metabolites specific of selected ions

768   from DESI-MSI were based on its assignment based on accurate mass and isotopic pattern score using

769   Progenesis software (Waters Inc., Milford, MA). The accurate mass search against the available databases

770   including Lipidmaps[35], HMDB(Wishart et al., 2022) and Metlin(Smith et al., 2005) for [M+ (H/Na/K)]$^+$

771   adducts were searched in positive ion mode and [M-H]$^-$ adducts in negative ion mode. For UPLC-HDMS^E

772   lipidomics data, the assignment of the lipid features was based on retention time information, accurate

773   mass as well as fragmentation information. Fragmentation match was made in Progenesis software, where

774   fragmentation score and match were assessed. It was also performed in MS^E dataviewer (Waters, Milford,

775   MA), where the fragments were confirmed against the lipidmaps structure database (LMSD)(Sud et al.,

776   2007) for the adducts mentioned above with mass tolerance of 5ppm. Finally, the accurate mass of DESI-

777   MSI based ion was matched against the UPLC-HDMS^E data for assignment.

778

779   **Successive SIMS imaging and data processing.**

780 **Cryogenic $(H_2O)_n$-GCIB-SIMS.** Both $(H_2O)_n$-GCIB and C_{60}-SIMS were performed on a buncher-ToF
781 instrument, J105 3D Chemical Imager (Ionoptika, Southampton, UK. Abbv. J105). The water cluster ion
782 beam is pulsed through a pulser in the gun column, where the distance to the sample surface is 0.533 m.
783 Beam tuning was assisted with an oscilloscope (Tektronix TDS 2024, USA) with detection by a secondary
784 electron detector (SED). The singly-charged $(H_2O)_n$ cluster size at beam energy of 70 kV with a time of
785 flight (ToF) of 103 µs was calculated using the ToF equation as n = 30,900 (Figure S15). The SED offset
786 was 8 µs. Beam focus was measured by scanning a 1000 mesh grid (Agar Scientific, Essex, UK). The
787 average beam spot sizes were calculated using 20/80 percent of maximum intensities and were 1.60±0.01
788 µm and 1.16±0.45 µm for 70 keV $(H_2O)_{30k}^+$ and 40 kV C_{60}^+, respectively (Figure S14). The beam dither
789 was adapted to match the image pixel size. The mass resolution m/Δm was 6875 around *m/z* 100, and
790 10,000~12,000 up to *m/z* 2000. The live readout of mass resolution was from the software, Ionoptika
791 SIMS Mainframe during the data acquisition.

792

793 The gold coated Si wafer with the frozen-hydrated mouse/human liver tissue section was plunged into
794 liquid nitrogen and inserted to the pre-chilled cold sample stage in J105 instrument and kept at 100 K
795 during GCIB-SIMS imaging. This cryogenic sample handling preserved the frozen-hydrated state thus
796 maintaining the chemical gradients in the tissue section.

797

798 Guided by the anatomical features on the semi-serial H&E stained section, an area of interest was selected
799 for SIMS imaging in negative ion mode using a 70 keV $(H_2O)_{30k}^+$ beam. The acquisition was in negative
800 ion mode with 256×256 pixels using a 2×2 tiled image mode for mouse liver tissue sections, or 768×768
801 pixels using a 3×3 tiled image mode for human liver tissue sections. Each tile covers 400×400 µm^2 (3.1
802 µm per pixel) for each section. With 1 pA of beam current and 296 shots per pixel, the ion doses were
803 3.01×10^{12} ions/cm^2 each tile.

804

805 **Immunostaining**. The antibody panel, designed to identify the major cell types, immune cells, cell
806 proliferation, structure and nuclei within the liver is described in Table S1 and S2. Briefly, after the
807 $(H_2O)_n$-GCIB-SIMS profiling was performed, the frozen tissue was placed at -20 °C and 4 °C
808 consecutively for 1 h each for temperature equilibration, followed by fixation in 4 % formalin solution at
809 4 °C for 30 min. Non-specific protein binding was blocked with 3 % BSA (Bovine Serum Albumin) for
810 45 min at room temperature. Overnight staining was then performed with the antibody cocktail solution

811 (750 ug/mL for each antibody) at 4 °C. The stained slide was washed with 0.2 % Triton X-100 in PBS

812 (phosphate-buffered saline) 1X for 8 min before the final nuclear staining with Intercalator-Ir at 300

813 µL/section. After washing with double-distilled water for 10 min and air-drying for 30 min, the slide was

814 again inserted into the SIMS instrument, this time for C60 imaging. For immunohistochemistry, briefly,

815 tissue sections were fixed in cold acetone, washed and incubated with 30% hydrogen peroxide. The

816 sections were blocked with 10% goat serum and incubated with primary antibody for 90 mins followed

817 by biotinylated secondary antibody at room temperature, with washing steps in between. This was

818 followed by addition of avidin-biotin complex reagent and then DAB (3,3′-Diaminobenzidine) with

819 washing between steps. The stained slide was washed with water and counterstained with hematoxylin,

820 mounted with coverslip and scanned at 20x resolution.

821

822 **C_{60}-SIMS.** High resolution images using 40 keV C_{60}^+ were then acquired on the same area previously

823 profiled by the $(H_2O)_n$-GCIB-SIMS. The acquisition was conducted in positive mode to localize various

824 cell types. This was achieved by spatially detecting unique *m/z* ions of the isotopic metal tags associated

825 with cell-specific antibodies. To resolve single cells, the C_{60}^+ beam was finely focused to 1.0 µm to image

826 roughly the same area which has been analyzed by $(H_2O)_n$-GCIB. With the beam current of 5 pA and 1000

827 shots per pixel, the ion dose was 8.57×10^{13} ions/cm^2. The dwell time was 100 ms/pixel. The lanthanide

828 tags from eight antibodies and the nuclear marker were detected at an adequate signal intensity to allow

829 co-registration with lipid and metabolite ions detected by $(H_2O)_n$-GCIB-SIMS.

830

831 **SIMS Data processing.** Single mass channels from tiled C_{60} and $(H_2O)_n$-GCIB-SIMS images were

832 extracted using [Ionoptika's Analyze] and subsequently used for downstream processing, all performed

833 with custom developed Python code. Co-registration of C_{60} and $(H_2O)_n$-GCIB-SIMS images was by first

834 selecting mass channels that demonstrated a representative morphology of the tissue and normalizing each

835 to an intensity range of [0, 1]. Normalized images were registered using SimpleITK(Beare et al., 2018) (v

836 2.0.2) to determine the best affine transform between the C_{60} (fixed) and H_2O (moving) images by

837 minimizing the mean square difference using a gradient descent optimizer (Figure S16). All H_2O channel

838 data was then transformed to the C_{60} image space. The general nuclear and membrane channels from the

839 C_{60} data set were then used to segment single cells using DeepCell(Bannon et al., 2021) (v 0.9.0). Since

840 the $(H_2O)_n$-GCIB-SIMS data has been registered to the C_{60} image space, the segmentation instances can

841 be used to extract integrated counts of species in both SIMS data sets. Integrated protein expression from

842   C_{60}-SIMS images was used to determine thresholds for cell classification (marker positive or negative)

843   (Figure S17). Hierarchical clustering analysis (HCA) was performed with seaborn (v 0.11.1) on the

844   integrated lipid and metabolite mass channels from the $(H_2O)_n$-GCIB-SIMS data set, using the cell types

845   determined from the C_{60} image data (Figure S18).

846

847   **MALDI-MSI.** Chemicals and solvents (analytical grade) were purchased from the following sources: α-

848   Cyano-4-hydroxycinnamic acid 98% (CHCA) (Sigma Aldrich), 1,5-Diaminonaphthalene 97% (DAN)

849   (Sigma Aldrich), acetonitrile (ACN) (Honeywell), chloroform (Acros Organics), methanol (Carl Roth),

850   and trifluoroacetic acid (TFA) (Sigma Aldrich). All chemicals used in this study were stored, handled,

851   and disposed of according to good laboratory practices (GLP).

852

853   Mouse and Human liver sections on ITO glass (Sigma, Milwaukee, WI, US) were stored at -80ºC until

854   analysis. Prior to matrix application, the tissue sections were removed from the freezer, placed on a cold

855   steel plate (-20ºC) and freeze-dried in a desiccator for 30 minutes. The combination of steel plate and

856   desiccator was efficient for removing the water from the tissue without compromising its structural

857   integrity and limiting the migration of analytes. On the mouse liver section, DAN matrix (10 mg/ml,

858   ACN:H_2O 7:3) was applied. For the analysis of human liver, 2 section were coated in matrix, one with

859   DAN (same as mouse) for negative ion mode and one with CHCA matrix (5mg/ml, $CHCl_3$:MeOH 1:1)

860   for positive ion mode analysis. Application was performed with an HTX TM sprayer (HTX Technologies

861   LLC, USA), temperature: 30ºC (Dan)/ 40ºC (CHCA), passes: 8 (DAN)/16 (CHCA), flow rate: 0.12

862   ml/min, velocity: 1200 mm/min, drying time: 2 s, line spacing 2.5 mm.

863

864   AP-MALDI analysis was performed using an AP-MALDI UHR ion source (Masstech Inc., USA), which

865   has been described in detail elsewhere,[40,41] coupled to an LTQ/Orbitrap Elite high-resolution mass

866   spectrometer (Thermo-Fisher Scientific, USA) in positive and negative ion mode. For imaging, the AP-

867   MALDI source was operated in "Constant Speed Raster" motion mode. To explore the detectable species

868   and instrument settings for both ion modes, one whole mouse liver section was analyzed interlaced in

869   positive and negative ion mode with a laser beam diameter of 20 µm and a stepping size of 50 µm, laser

870   settings 2500 Hz, 5%. Spectrum acquisition parameters were 800 ms maximum injection time, mass range:

871   500 – 2000 Da and mass resolution: 120k at m/z 400. Human liver was analyzed with higher spatial

872   resolution (15 µm laser spot and stepping size) and positive (CHCA matrix, laser settings 500 Hz, 10%)

873 and negative (DAN matrix, laser settings 1500 Hz, 5%) ion mode analysis was performed on 2 separate,

874 consecutive sections. Spectrum acquisition was adjusted to 500 ms maximum injection time, mass range:

875 350 – 1550 Da and mass resolution: 120k at m/z 400. Species identification was performed with on-tissue

876 tandem-MS with a 1.5 Da isolation window, and collision-induced dissociation/ higher-energy collision

877 dissociation (CID/HCD) was performed with collision energies of 27-45%, adjusted for each species

878 individually. Tandem-MS scans were summed up over 30-120 seconds. Data analysis and visualization

879 was performed with Thermo Xcalibur 2.2 (Thermo-Fisher Scientific, USA), MultimagingTM

880 (ImaBiotech, France), METASPACE,[42] and LipostarMSI (Molecular Horizons Srl, Italy).[43] Lipid

881 identification was performed in LipostarMSI (database: LIPIDMAPS, mass accuracy: 2 ppm; mass and

882 isotopic pattern score: 80%+).

883

884 **RNAScope.** We captured transcription distributions of select liver cell marker genes via *in situ*

885 hybridization of specific targeting probes with the RNAscope Multiplex Fluorescent v2 Assay Protocol[27]

886 optimized for fresh-frozen samples. Our modifications to the commercial protocol included using half-

887 concentration wash buffer (0.5X) for all wash steps downstream of probe incubation, and excluding the

888 recommended protease step entirely. In mouse tissue, we spatially detected the transcripts for, ALB

889 (Albumin), GLUL (Glutamine synthetase), and PTPRC (Protein Tyrosine Phosphatase Receptor Type C),

890 and in human tissue, we spatially detected transcripts for GLUL, CD68 (Macrophage Antigen CD68), and

891 LYVE1 (Lymphatic Vessel Endothelial Hyaluronan Receptor 1).

892

893 Tissue sections were first post-fixed with 4% paraformaldehyde (PFA) in phosphate buffered saline (PBS)

894 and dehydrated in Ethanol (EtOH) immediately after fixation, immersed for 5 minutes at a time in 50%

895 EtOH, 70% EtOH, 100% EtOH, and 100% EtOH an additional time. Samples were then air-dried and

896 treated with RNAscope® Hydrogen Peroxide Reagent for ten minutes at 23°C to 25°C and washed twice

897 with deionized water. Importantly, we excluded the commercial protease step because tissue integrity was

898 lost, and we could achieve stronger signal without any protease treatment. These steps constitute the

899 pretreatment steps.

900

901 These pretreated sample slides were incubated with prewarmed target probes (20 nmol/L of each oligo

902 probe) overnight. In mouse tissue, ALB was targeted with RNAscope® Probe- Mm-Alb-C2 (ACD;Cat

903 No. Cat No. 437691-C2), GLUL was targeted with RNAscope Probe- Mm-Glul (ACD;Cat No. 426231),

904 and PTPRC was targeted with RNAscope® Probe- Mm-Ptprc-C3 (ACD;Cat No. 318651-C3). In human

905 tissue, GLUL was targeted with RNAscope® Probe- Hs-GLUL-No-XMm (ACD;Cat No. Cat No.

906 511171), CD68 was targeted with RNAscope® Probe- Hs-CD68-C4 (ACD;Cat No. 560591-C4), and

907 LYVE1 was targeted with RNAscope® Probe- Hs-LYVE1 (ACD;Cat No. 426911).

908

909 The tissue was incubated in the primary target probes overnight (18-21 hours) at 40°C inside the HybEZ

910 hybridization oven (ACD). After overnight probe hybridization, samples were incubated in Amplifier 1

911 (preamplifier) (2 nmol/L) in hybridization buffer B (20% formamide, 5× SSC, 0.3% lithium dodecyl

912 sulfate, 10% dextran sulfate, blocking reagents) for 30 minutes; Amplifier 2 (2 nmol/L) in hybridization

913 buffer B at 40°C for 15 minutes; and Amplifier 3 (label probe) (2 nmol/L) in hybridization buffer C (5×

914 SSC, 0.3% lithium dodecyl sulfate, blocking reagents) for 15 minutes. After each hybridization step, slides

915 were washed with 0.5X wash buffer (0.05× SSC, 0.015% lithium dodecyl sulfate) two times at room

916 temperature. Chromogenic detection was performed utilizing a horseradish peroxidase (HPR) construct

917 specific to each gene-dedicated imaging channel and a fluorescent Opal reagent of choice. For the mouse

918 sections, ALB was stained with Opal 520 Reagent (Perkin Elmer, FP1487001KT), GLUL was stained

919 with Opal 570 Reagent (Perkin Elmer, FP1488001KT), and PTPRC was stained with Opal 690 Reagent

920 (Perkin Elmer, FP1488001KT). For the human sections, GLUL and LYVE1 were both stained with Opal

921 520 Reagent (Perkin Elmer, FP1487001KT), thus needing to be imaged in separate tissue sections, and

922 CD68 was stained with Opal 570 Reagent (Perkin Elmer, FP1488001KT). Each Opal reagent dye was

923 diluted 1:1500 in RNAscope® Multiplex TSA Buffer. Nuclei were stained with DAPI (4′,6-diamidino-2-

924 phenylindole) and coverslips were mounted over slides in Fluoro-Gel (EMS; 17985-10) and imaged by

925 spinning disc confocal microscopy and Aperio Versa 8 fluorescent slide scanner.

926

927 **Reference**

928 Bannon, D., Moen, E., Schwartz, M., Borba, E., Kudo, T., Greenwald, N., Vijayakumar, V., Chang, B.,
929 Pao, E., Osterman, E., *et al.* (2021). DeepCell Kiosk: scaling deep learning-enabled cellular image
930 analysis with Kubernetes. Nat Methods *18*, 43-45.
931 Beare, R., Lowekamp, B., and Yaniv, Z. (2018). Image Segmentation, Registration and Characterization
932 in R with SimpleITK. J Stat Softw *86*.
933 Kessner, D., Chambers, M., Burke, R., Agus, D., and Mallick, P. (2008). ProteoWizard: open source
934 software for rapid proteomics tools development. Bioinformatics *24*, 2534-2536.
935 Race, A.M., Styles, I.B., and Bunch, J. (2012). Inclusive sharing of mass spectrometry imaging data
936 requires a converter for all. J Proteomics *75*, 5111-5112.

937 Smith, C.A., O'Maille, G., Want, E.J., Qin, C., Trauger, S.A., Brandon, T.R., Custodio, D.E., Abagyan,
938 R., and Siuzdak, G. (2005). METLIN: a metabolite mass spectral database. Ther Drug Monit *27*, 747-
939 751.
940 Sud, M., Fahy, E., Cotter, D., Brown, A., Dennis, E.A., Glass, C.K., Merrill, A.H., Jr., Murphy, R.C.,
941 Raetz, C.R., Russell, D.W.*, et al.* (2007). LMSD: LIPID MAPS structure database. Nucleic Acids Res
942 *35*, D527-532.
943 Wishart, D.S., Guo, A., Oler, E., Wang, F., Anjum, A., Peters, H., Dizon, R., Sayeeda, Z., Tian, S., Lee,
944 B.L.*, et al.* (2022). HMDB 5.0: the Human Metabolome Database for 2022. Nucleic Acids Res *50*,
945 D622-D631.

946

947 **KEY RESOURCES TABLE**

REAGENT or RESOURCE				SOURCE	IDENTIFIER
Antibodies for mouse liver					
Metal tag	**Target**	**Clone/Host**	**Cell/Pathway**		**Manufacturer/Catalog No.**
89Y	CD45	30-F11, Rat IgG2b	Pan leukocyte		Fluidigm/3089005B
142Nd	Heppar-1/CPS1	HepPar1, mouse monoclonal	Periportal hepatocytes (Zone 1)		Novus/NBP3-08970
143Nd	GFAP	EPR1034Y, Rabbit monoclonal	Ito Stellate Cells		Abcam/ab218309
147Sm	GS	ab240193,Rabbit monoclonal	Pericentral hepatocytes (Zone 3)		Abcam/ab240193
152Sm	F4/80	CI:A3-1, Mouse IgG2b	Kupffer cells		Abcam/ab6640
155Gd	CD11b	M1/70, Rat IgG	Leukocytes		Ionpath/ 715503-100
156Gd	CD68	FA-11, Mouse IgG2b	Macrophages		Abcam/ ab237968
174Yb	LYVE1	Rabbit polyclonal	Sinusoidal endothelial cells		Novus/ NB600-1008
176Yb	EGFR	EP38Y, Rabbit monoclonal	Cell membrane		Abcam/ ab272293
176Yb	Na/K ATPase	EP1845Y, Rabbit monoclonal	Cell membrane		Abcam/ab167390
191 Ir	Nuclear DNA		Nuclei		Fluidigm/ 201192B
Antibody for Human liver					
Metal tag	**Target**	**Clone/Host**	**Cell/Pathway**		**Manufacturer/Catalog No.**
89Y	CD45	D9M8I, Rabbit IgG	Pan leukocyte		Cell Signaling/13917S
113 In	CD4	RPA-T4, mouse monoclonal	T cells and macrophages		Novus/NBP2-25199
141Pr	SMA	1A4, Mouse IgG2a	Smooth muscle cells in vascular walls, sinusoildal endothelial cells and activated fibroblasts		Fluidigm/3141017D
143Nd	GFAP	EPR1034Y, Rabbit monoclonal	Ito Stellate Cells		Abcam/ab218309
145Nd	Heppar-1/CPS1	HepPar1, mouse monoclonal	Periportal hepatocytes (Zone 1)		Novus/NBP3-08970
147Sm	GS	ab240193,Rabbit monoclonal	Pericentral hepatocytes (Zone 3)		Abcam/ab240193
148Nd	CD31	JC/70A, Mouse monoclonal	Endothelial cells		Abcam/ab264090
151Eu	CD68	D4B9C,Rabbit IgG	Macrophages		Cell Signaling/76437S

153Eu	CD32	FUN-2, Mouse IgG2b	B cells, monocytes, granulocytes and platelets	Fluidigm/3153018B
158Gd	Arginase1	D4E3M™,Rabbit IgG	Zone 1-2 hepatocytes, and macrophages	Cell Signaling/93668S
161Dy	Albumin	EPR20195, Rabbit monoclonal	Periportal hepatocytes (Zone 1)	Abcam/Ab271979
166Er	CK19	SPM561, Mouse monoclonal	Cholangiocytes (Portal triad)	Abcam/ab212569
169Tm	CD34	QBEND/10, Mouse / IgG1	Endothelial cells	Abcam/ ab198395
170 Er	EpCAM	E6V8Y, Rabbit IgG	Hepatic stem/progenitor cells	Cell Signaling /93790S
171Yb	LYVE1	EPR21857, Rabbit monoclonal	Sinusoidal endothelial cells and subsets of macrophages	Abcam/ab232935
176Yb	EGFR	EP38Y, Rabbit monoclonal	Cell membrane	Abcam/ ab272293
176Yb	Na/K ATPase	D4Y7E, Rabbit IgG	Cell membrane	Cell Signaling/ 23565S
191 Ir	Nuclear DNA		Nuclei	Fluidigm/ 201192B
196Pt	Collagen I	EPR7785, Rabbit monoclonal	Connective tissue around portal triad	Abcam/ab215969
Biological samples				
Health mouse liver			17 weeks old male (n=3) and female (n=3) C57/BL6 mice	
Health human liver		Columbia University tissue bank	51-year-old female	
Deposited data				
SIMS raw date		This paper	doi:10.26207/6a38-tr35	
DESI raw date		This paper		
mRNA scope raw date		This paper		
Software and algorithms				
Ionoptika Image Analyzer		Ionoptika Ltd.	https://ionoptika.com	
ImagingSIMS		Jay Tarolli	https://github.com/Imaging SIMS/ImagingSIMS	
DeepCell		Bryan Chan, et al	https://deepcell.com/	
SCiLS		Bruker Corp.	https://www.bruker.com/	
Progenesis		Waters Corp.	https://www.waters.com/	
MS^E dataviewer		Waters Corp.	https://www.waters.com/	
Other				

948

949

950

951

952

953

954

955

956

957

958

959

960

961

962

963

964

965

966

967

968

969

970

971

972

973

974

975

976

977

978
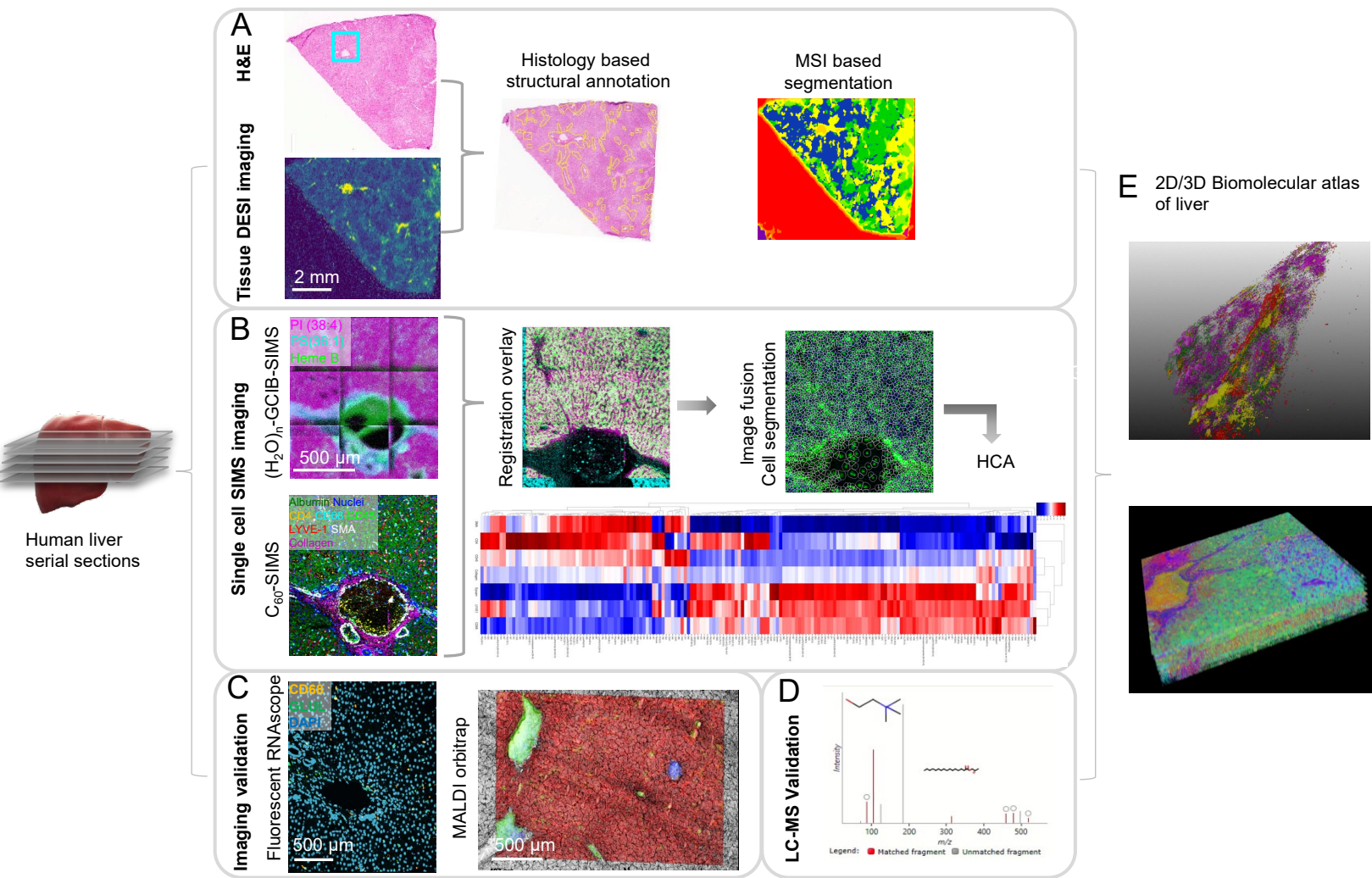
Figure 1. Schematics of MSI-centric multimodal imaging workflow reveals 2D/3D biomolecular atlas of human liver. Consecutive sections from liver tissue blocks are assessed by **A,** DESI-MSI exhibiting the distribution of lipids and metabolites within histologically defined structural units of liver within the tissue architecture and **B,** SIMS-MSI including $(H_2O)_n$-GCIB-SIMS for lipid and metabolite imaging at single cell resolution followed by C_{60}-SIMS on the same tissue section, followed by image integration and single cell specific lipid and metabolite extraction **C,** Validation of lipids detected by DESI and SIMS and **D,** structural elucidation by UPLC-MS^E lipidomics on liver tissue section homogenate **E,** The 2D images from DESI and SIMS are aligned for 3D reconstruction and visualization.
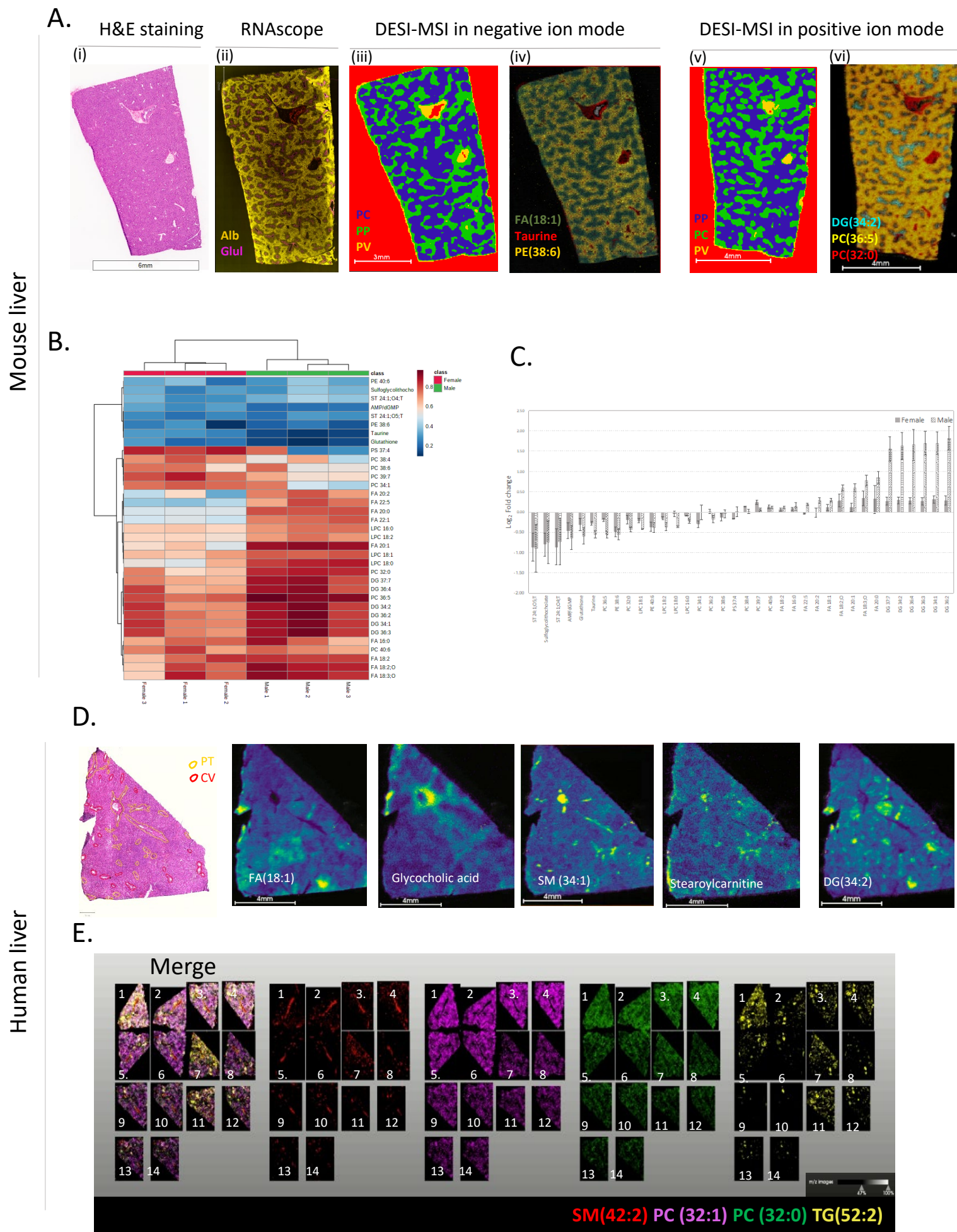
**Figure 2. DESI MSI reveals periportal and pericentral specific lipids and metabolites in mouse and human liver. Ai,** H&E staining performed on a normal mouse liver section to identify the central vein (CV) and portal triad (PT) regions. **Aii**, RNAScope is performed on a consecutive tissue section stained for expression of Albumin (Alb-yellow) and Glutamine Synthetase (Glul- magenta) showing differential staining for periportal (PP) and pericentral (PC) regions respectively**. Aiii**, **Av**, Spatial segmentation of pixels based on distribution of a few lipids and metabolites from DESI-MSI in (Aiii) negative and (Av) positive ion mode. (Aiv, Avi) Distribution of a few lipids and metabolites showing PC and PP specificity in both ion modes are shown. **B,** Heatmap depicting the predictive performance of features measured by AUC-ROC (in rows) and classification (in columns) from DESI for PP and PC regions in female (n=3) and male (n=3) mice liver sections. **C,** Fold change values comparing the mean intensity of PC versus PP regions for the features from (B) Error bars represent mean $\pm$ standard deviation. **D,** H&E section with manual annotation of CV and PT regions in human liver section. The corresponding images for distribution of different classes of lipids are shown. **E,** Distribution of lipids in consecutive sections for 3-dimensional visualization of lipids as shown in Supp video1.
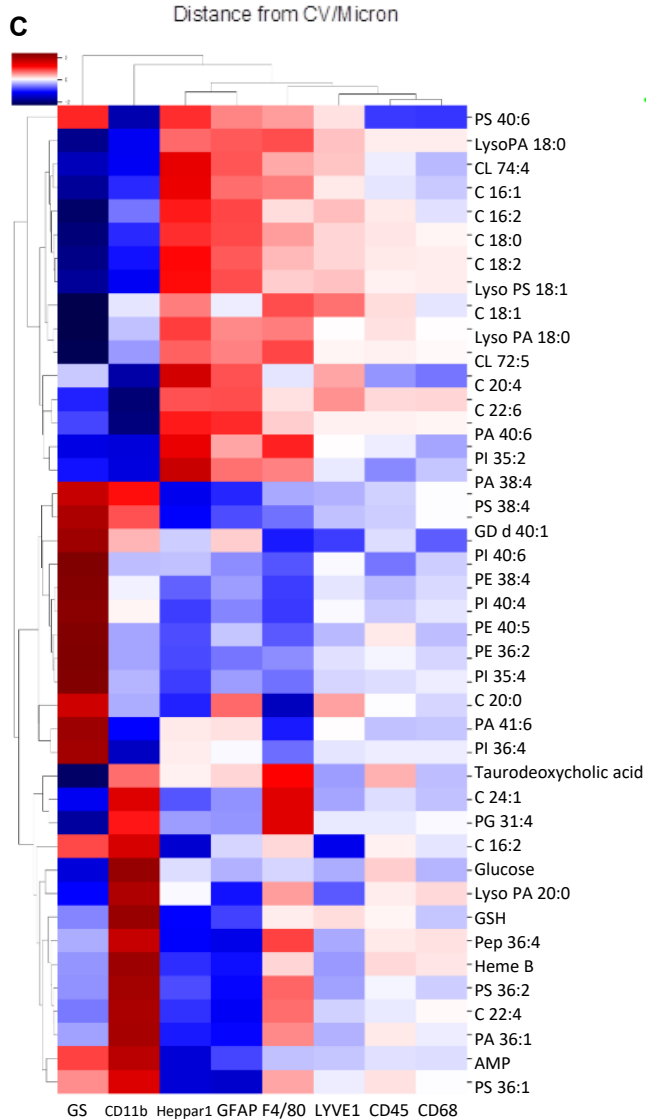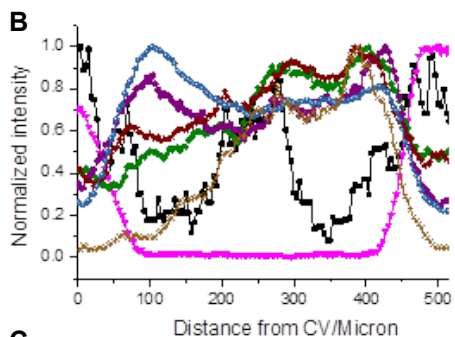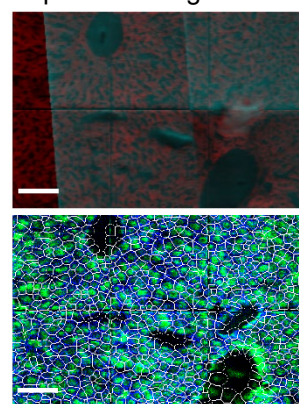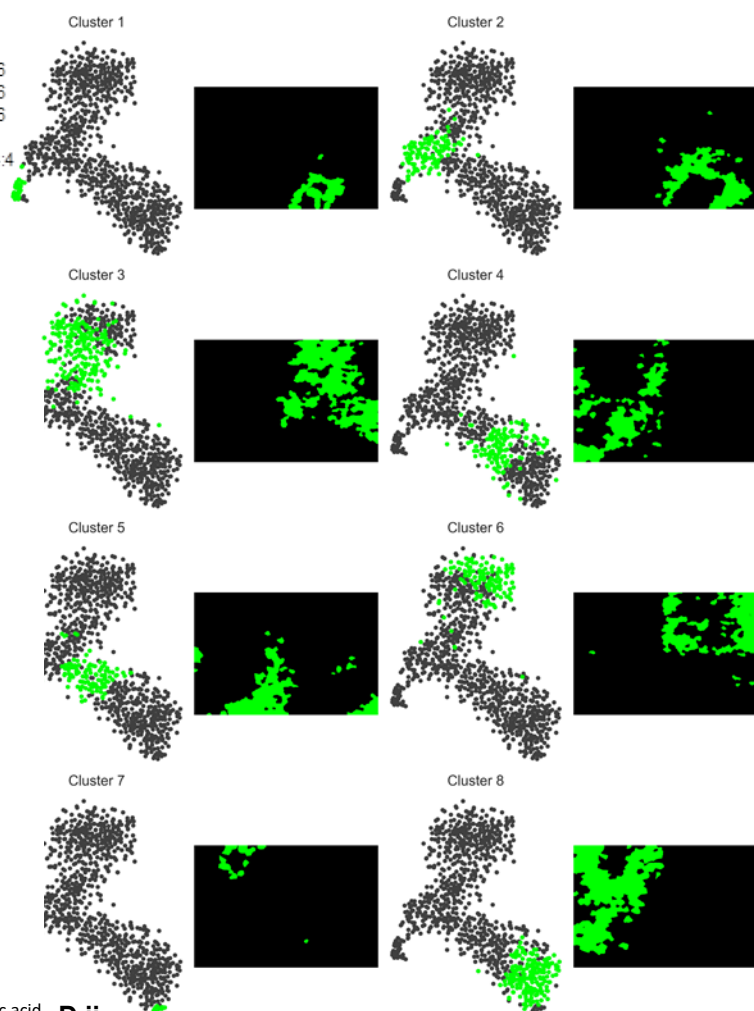
A i H&E image of ROI
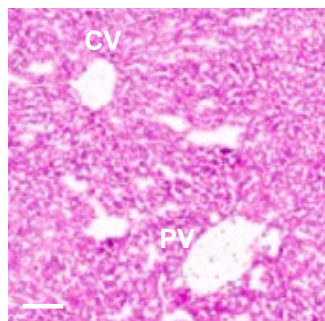
A ii $(H_2O)_n$-GCIB-SIMS for lipids/metabolites
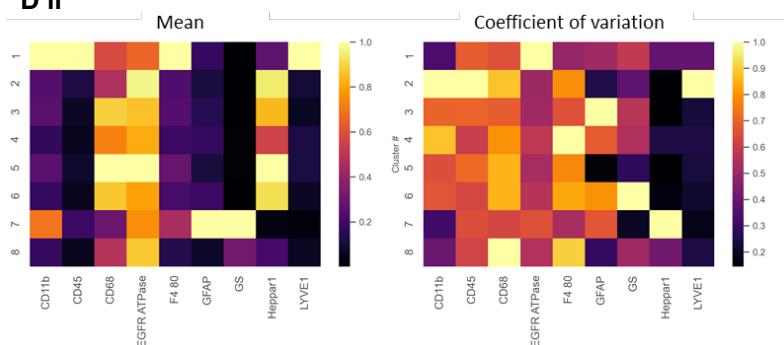C_{60}-SIMS for proteins on the same tissue
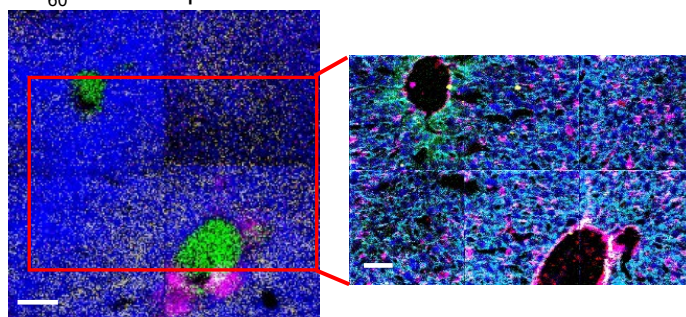
A iii Image registration
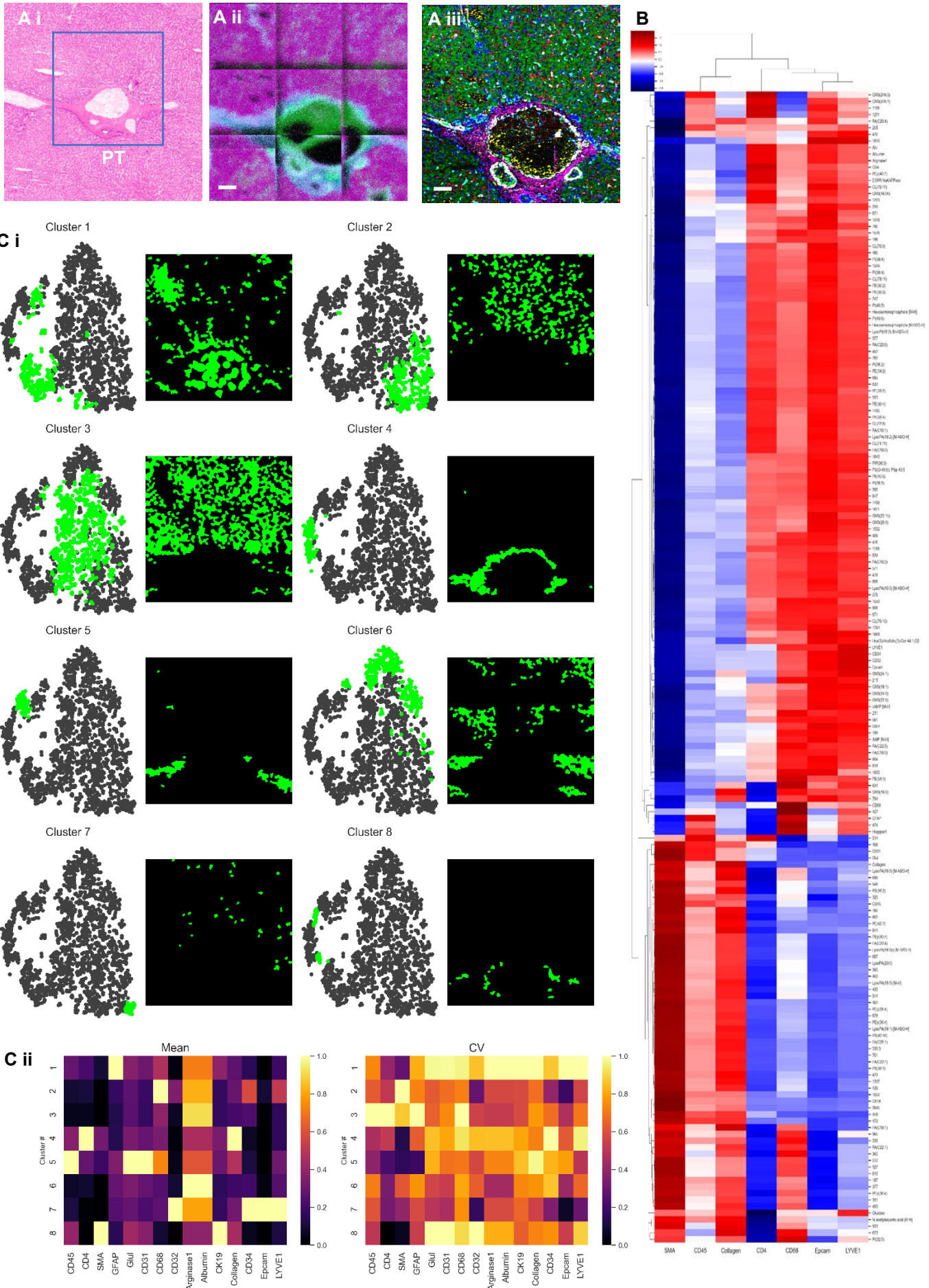DeepCell cell segmentation

B

C

D i

D ii

Figure 3 Dual high-resolution SIMS imaging delineates the metabolomic and lipidomic states in different cell types on the mouse liver section. Ai, H&E staining image of central vein (CV) and portal vein (PV) region. **Aii**, Representative color overlay images of Dual-SIMS. Metabolites and lipids image in the same region as in Ai on a serial frozen-hydrated section using $(H_2O)_{n(n=30k)}$-GCIB-SIMS at the spatial resolution of 3 μm, Blue, PI 38:4; Magenta, Taurocholic acid ; Yellow, PS 40:6; Green, HEME B. More single specie images are in Figure S6. Proteins image by lanthanides-conjugated antibodies from the region highlighted in the red box using C_{60}-SIMS at the spatial resolution of 1 μm, Red, CD45 and CD11b; Yellow, GFAP; White, LYVE-1; Magenta, F4/80 and CD68; Cyan, EGFR and Na/KATPase; Green, Glul; Blue, Nuclei. Scale bar 100 μm. **Aiii**, Registration of dual-SIMS images for alignment; Single cell segmentation using DeepCell. More details are described in supplementary Figures S16 and S17. **B**, Intensities changes of various species from the center of CV to PV (as the blue line in A i). **C**, HCA map shows the variation of different metabolites/lipids in various types of cells. **Di**, tSNE clustering to classify the cell types as in cluster 1-8 by lipids and metabolites only. **Dii**, Correlation of cluster 1-8 to 9 protein markers.

Figure 4. Dual high-resolution SIMS imaging delineates the metabolomic and lipidomic states in different cell types on the human liver tissue section. Ai, H&E image. The selected region contains the central vein and portal vein. **Aii**, Representative color overlay images of Dual-SIMS. Metabolites and lipids image in the same region as in Ai on a serial frozen-hydrated section using $(H_2O)_{n(n=30k)}$-GCIB-SIMS at the spatial resolution of 3 μm, Blue, PS 36:1; Magenta, PI 38:4; Green, HEME B. More single specie images are in Figure S10. Proteins image by lanthanides-conjugated antibodies from the same region after $(H_2O)_{n(n=30k)}$-GCIB-SIMS using C_{60}-SIMS at spatial resolution of 1 μm, Red, CD45 and CD11b; Magenta, GFAP; White, LYVE-1; Yellow, Heppar-1; Cyan, EGFR and Na/KATPase; Green, Glul; Blue, Nuclei. **Aiii**, The image alignment and registration of dual-SIMS images (i.e., Aii and Aiii). More details are described in supplementary Figures S16 and S17. **B**, HCA map shows the variation of different metabolites/lipids in different types of cells. **Ci**, tSNE clustering to classify the cell types as in cluster 1-8 by lipids and metabolites only. **Cii**, Correlation of cluster 1-8 to 15 protein markers.

Table 1. Validation of lipid ion species from SIMS and DESI-MSI with MALDI-MSI and LC-MS/MS

Pericentral vein region				Periportal vein region			
$(H_2O)_n$-GCIB-SIMS negative ion mode	MALDI Orbitrap validation	LC-MS precursor mass	LC-MS/MS validation	$(H_2O)_n$-GCIB-SIMS negative ion mode	MALDI Orbitrap validation	LC-MS precursor mass	LC-MS/MS validation
303.23 FA C20:4	NA	NA	NA	255.23 FA C16:0	NA	NA	NA
311.23 FA C20:0	NA	NA	NA	279.23 FA C18:2	NA	NA	NA
742.53 PE 36:2	PE(18:0/18:2)	NA	NA	283.26 FA C18:0	NA	NA	NA
766.54 PE 38:4	PE(18:0/20:4)	NA	NA	514.28 Taurocholic acid	NA	NA	NA
911.56 PI 40:5	PI(18:0/22:5)	NA	NA	747.50 PA 40:6	PA(18:0/22:6)	747.48	PA 40:6
913.58 PI 40:4	PI 40:4	NA	NA	834.53 PS 40:6	PS(18:0/22:6)	834.53	PS 40:6
857.51 PI 36:4	PI(16:0/20:4)	NA	NA	835.53 PI 34:1	PI(12:0/22:1(11Z))	835.53	PI 34:1
723.50 PA 38:4	PA(18:0/20:4)	723.48	PA 18:2/20:2	1454.03 CL 72:5	NA	NA	NA
810.53 PS 38:4	PS(18:0/20:4)	810.54	PS 38:4	1455.95 CL 72:4	NA	NA	NA
812.54 PS 38:3	NA	812.55	PS 38:3	1480.94 CL 74:6	NA	NA	NA
885.55 PI 38:4	PI(18:0/20:4)	885.55	PI 38:4	1482.08 CL 74:5	NA	NA	NA
				1483.94 CL 74:4	NA	NA	NA
				1484.98 CL 74:4	NA		
DESI negative ion mode	MALDI Orbitrap validation	LC-MS precursor mass	LC-MS/MS validation	DESI negative ion mode	MALDI Orbitrap validation	LC-MS precursor mass	LC-MS/MS validation
281.24 FA 18:1	NA	NA	NA	124.01 Taurine	NA	NA	NA
295.23 FA 18:2;O	NA	NA	NA	306.08 GSH	NA	NA	NA
293.21 FA 18:3;O	NA	NA	NA	762.51 PE 38:6	NA	762.50	PE 38:6
309.28 FA 20:1	NA	NA	NA	346.05 AMP/dGMP	NA	NA	NA
311.3 FA 20:0	NA	NA	NA	175.03 Ascorbic acid	NA	NA	NA
307.26 FA 20:2	NA	NA	NA	514.28 ST 24:1;O5;T	NA	NA	NA
				512.27 Sulfoglycolithocholate	NA	NA	NA
				498.29 ST 24:1;O4;T	NA	NA	NA
				790.53 PE 40:6	PE(18:0/22:6)	790.53	PE 40:6
DESI positive ion mode	MALDI Orbitrap validation	LC-MS precursor mass	LC-MS/MS validation	DESI positive ion mode	MALDI Orbitrap validation	LC-MS precursor mass	LC-MS/MS validation
647.46 DG 37:7	NA	647.45	DG 37:7	818.50 PC 36:5	PC 36:5	NA	NA
840.55 PC 39:7	NA	840.55	PC 39:7	756.54 PC 32:0	PC 34:3	756.54	PC 32:0
848.54 PC 38:4	PC 38:4	848.55	PC 38:4	560.31 LPC 18:1	NA	NA	NA
633.48 DG 34:1	NA	633.48	DG 34:1	562.32 LPC 18:0	PC 18:0	NA	NA
631.46 DG 34:2	NA	631.46	DG 34:2	518.32 LPC 16:0	PC 16:0	NA	NA
659.49 DG 36:2	NA	659.49	DG 36:2	760.58 PC 34:1	PC 34:1	NA	NA
657.48 DG 36:3	NA	657.48	DG 36:3	806.56 PC 38:6	PC 36:3	NA	NA
655.46 DG 36:4	NA	655.46	DG 36:4	542.32 LPC 18:2	NA	NA	NA
856.56 PC P-40:6	NA	856.55	PC P-40:6	786.59 PC 36:2	PE(36:2)	786.59	PC 36:2